Implementation of Warm-Cloud Processes in a Source-Oriented WRF/Chem Model to Study the Effect of Aerosol Mixing State on Fog Formation in the Central Valley of California

Hsiang-He Lee[1*], Shu-Hua Chen[1@], Michael J. Kleeman[2], Hongliang Zhang[2], Steven P. DeNero[2], and David K. Joe[2]

[1] Department of Land, Air, and Water Resources, University of California, Davis, CA

[2] Department of Civil & Environmental Engineering, University of California, Davis, CA

Submitted to

Atmospheric Chemistry and Physics

October 18, 2015

[@]Corresponding author address: Dr. Shu-Hua Chen, Department of Land, Air, and Water Resources, University of California, Davis, California 95616-8627.
E-mail: shachen@ucdavis.edu

*now at: Singapore-MIT Alliance for Research and Technology (SMART), Centre for Environmental Sensing and Modeling (CENSAM), Singapore

Abstract

The source-oriented Weather Research and Forecasting chemistry model (SOWC) was modified to include warm cloud processes and applied to investigate how aerosol mixing states influence fog formation and optical properties in the atmosphere. SOWC tracks a 6-dimensional chemical variable (X, Z, Y, Size Bins, Source Types, Species) through an explicit simulation of atmospheric chemistry and physics. A source-oriented cloud condensation nuclei module was implemented into the SOWC model to simulate warm clouds using the modified two-moment Purdue Lin microphysics scheme. The Goddard shortwave and longwave radiation schemes were modified to interact with source-oriented aerosols and cloud droplets so that aerosol direct and indirect effects could be studied.

The enhanced SOWC model was applied to study a fog event that occurred on 17 January 2011, in the Central Valley of California. Tule fog occurred because an atmospheric river effectively advected high moisture into the Central Valley and nighttime drainage flow brought cold air from mountains into the valley. The SOWC model produced reasonable liquid water path, spatial distribution and duration of fog events. The inclusion of aerosol-radiation interaction only slightly modified simulation results since cloud optical thickness dominated the radiation budget in fog events. The source-oriented mixture representation of particles reduced cloud droplet number relative to the internal mixture approach that artificially coats hydrophobic particles with hygroscopic components. The fraction of aerosols activating into CCN at a supersaturation of 0.5% in the Central Valley decreased from 94% in the internal mixture model to 80% in the source-oriented model. This increased surface energy flux by 3-5 W m^{-2} and surface temperature by as much as 0.25 K in the daytime.

1. Introduction

Atmospheric aerosols are complex mixtures of particles emitted from many different anthropogenic and natural sources suspended in the atmosphere. In contrast to greenhouse gases, aerosols have large spatial and temporal variability in the troposphere because of their short lifetimes (about one week) before coagulation, dry deposition, or wet scavenging processes remove them from the atmosphere (Ramanathan et al., 2001). Aerosol particles can influence human health (McMichael et al., 2006), ecological health (over land and ocean) (Griffin et al., 2001), visible range through the atmosphere (Dick et al., 2000), cloud / precipitation formation (Chen et al., 2008), and the net radiation budget of the earth (IPCC, 2007). Some chemical components of aerosol particles are important to direct radiative forcing of the climate due to their optical properties (Tegen et al., 1996). Particulate sulfate scatters incoming solar radiation, leading to an estimated direct forcing of -0.95 W m^{-2} (Adams et al., 2001). Particulate black carbon strongly absorbs incoming shortwave radiation, which warms the mid-level of the atmosphere but cools the earth's surface (Yang et al., 2009; Koch and Del Genio, 2010). Particulate black carbon also leads to reduce relative humidity and cloud liquid water content (semi-direct effect) in the mid-level atmosphere (Ackerman et al., 2000; Koch and Del Genio, 2010). In addition to these direct effects, Twomey (1974) proposed that aerosols indirectly affect the earth's energy budget due to their ability to serve as cloud condensation nuclei (CCN), which are of great importance in cloud development, especially for warm clouds in the mid-to-high latitudes. Large numbers of CCN produce clouds with a greater number of smaller size cloud droplets (Chen et al., 2008). These smaller cloud droplets raise cloud albedo (the first indirect effect) and also suppress the formation of precipitation and prolong cloud lifetime (the second indirect effect) (Albrecht, 1989). The direct, semi-direct, and indirect effects of aerosol particles

75 modify the energy budgets in the atmosphere and on the surface, with corresponding changes in
76 atmospheric stability. The 2007 IPCC report (IPCC, 2007) concluded that the net forcing of all
77 aerosols could be either positive or negative in the range from -0.7 W m^{-2} to +0.1 W m^{-2}. The
78 majority of this uncertainty is associated with the semi-direct and indirect effects due to the
79 complexity of aerosol-cloud interactions.

80 The magnitude of the aerosol semi-direct and indirect effects depends on the number
81 concentration, size, and composition of the atmospheric aerosol particles that act as CCN or ice
82 nuclei (IN) (Lohmann and Feichter, 2005; Chen et al., 2008). Particles with hygroscopic
83 components such as water-soluble ions (Na^+, Cl^-, SO_4^{2-}, NO_3^- etc.) readily act as CCN (Chen and
84 Lamb, 1994). Particles that contain hydrophobic components such as freshly emitted organic
85 carbon or elemental carbon must become coated with hygroscopic material before they will
86 easily serve as CCN (Dusek et al., 2006). Some studies showed the importance of the aerosol
87 mixing state on CCN activation using field campaign data and numerical modeling. Cubison et
88 al. (2008) focused on the relationship between the CCN number concentration and the physical
89 and chemical properties of aerosols in the urban area in California. Based on the results from a
90 cloud parcel model and observed CCN number, they found that a realistic treatment of the
91 mixing state of the urban aerosol distribution is critical to the CCN activation prediction. Anttila
92 (2010) also used an adiabatic cloud parcel model to investigate the importance of the particle
93 mixing state and hygroscopicity to CCN activation. They commented that the differences
94 between externally and internally mixed aerosols in urban and rural environments could reach up
95 to 35%. Both modeling studies investigated the effect of aerosol mixing state on CCN formation
96 based on an ideal cloud parcel model. While observations from Ma et al. (2010) and Lance et al.
97 (2013) showed consistent results with these modeled CCN studies, a more sophisticated 3-

98 dimational numerical model is needed to further study this issue. Mineral dust particles (Motoi,
99 1951; Georgii and Kleinjung, 1967) commonly have a favorable arrangement of surface structure
100 that allows them to serve as IN. Secondary coatings that condense on mineral dust particles may
101 reduce their ability to serve as IN (Sullivan et al., 2010) but increase their ability to serve as CCN
102 (Li and Shao, 2009). From the IPAC-NC (Influence of Pollution on Aerosols and Cloud
103 Microphysics in North China) field campaign data, Ma et al. (2010) showed that dust particles
104 can become the predominant source of CCNs in a few hours after being coated by high pollution
105 acids. This aging process has been parameterized in numerical models (Lesins et al., 2002) but
106 how the aging timescale should respond to changes in temperature, humidity, oxidant
107 concentrations and/or emissions rates is not described in most models. All of these mentioned
108 above point to the importance of the particle mixing state when predicting CCN / IN
109 concentrations.

110 The standard Weather Research and Forecasting (WRF) model, including the chemistry
111 component (WRF/Chem), permits the simulation of the combined direct, indirect and semi-direct
112 effects of aerosols (Chapman et al., 2009; Fast et al., 2006; Grell et al., 2005). WRF/Chem
113 Version 3.1.1 has sophisticated packages to represent chemistry processes (i.e. gas-phase
114 reaction, gas-to-particle conversion, coagulation, etc.) and aerosol size and composition (Zaveri
115 et al., 2008; Ackermann et al., 1998; Binkowski and Shankar, 1995; Schell et al., 2001). The
116 Modal Aerosol Dynamics Model for Europe with Secondary Organic Aerosol Model (MADE-
117 SORGAM) and the Model for Simulating Aerosol Interactions and Chemistry (MOSAIC) are
118 commonly used aerosol schemes in the WRF/Chem model. Both schemes have inorganic,
119 organic, and secondary organic aerosols and contain aerosol formation processes including
120 nucleation, condensation, and coagulation. The main difference between MADE-SORGAM and

MOSAIC is the representation of aerosol size distributions. MADE-SORGAM uses 3 log-normal modes (Aitken, accumulation and coarse) while MOSAIC uses 4 (or 8) aerosol size sections (bins) from 39 nm to 10 μm, respectively. The details of MADE-SORGAM are described in Binkowski and Shankar (1995), Ackermann et al. (1998), Schell et al. (2001), and Grell et al. (2005) and the details of MOSAIC are given in Zaveri et al. (2008).

As mentioned above, the size, composition, and mixing state of aerosols strongly affect their ability to activate into cloud droplets (Lance et al., 2013; Zaveri et al., 2010). However, most WRF/Chem chemistry packages make a global internal mixing assumption in which all particles within a log-normal mode (MADE-SORGAM) / size bin (MOSAIC scheme) in the same grid cell are instantaneously combined such that they have the same chemical composition. In reality, airborne particles are emitted with unique chemical composition and only become internally mixed over a period of hours to days depending on atmospheric conditions. The instantaneous internal mixing assumption alters the optical and chemical properties of particles in WRF/Chem simulations (Zhang et al., 2014) and therefore has the potential to influence aerosol-cloud interaction (i.e. CCN activation).

The primary goal of this research is to quantify the effect of assumptions about particle mixing state on predicted cloud droplet formation within the WRF/Chem model. Warm cloud processes in the Purdue Lin scheme (Chen and Sun, 2002) were modified in the Source-Oriented WRF/Chem (SOWC) model to investigate the impact of aerosol mixing state on the characteristics of a fog event in the Central Valley of California. The SOWC model explicitly predicts particle mixing state in the presence of emissions, transport, coagulation, chemical transformation, and deposition. The integration of warm-cloud processes with the source-

oriented treatment of particles in the current study provides a more realistic approach to understand how mixing state influences direct, indirect, and semi-indirect effects of anthropogenic aerosols.

This paper is organized as follows: the model description and development of warm cloud processes are introduced in section 2; observational data and numerical experiment design are presented in section 3; results are discussed in section 4; and the summary and discussion are provided in section 5.

2. Model Description and Development

2.1 SOWC

WRF is a compressible, non-hydrostatic regional meteorology model, which uses the Arakawa C grid and terrain-following hydrostatic pressure coordinates. The governing equations of the model are written in flux form and can be solved using a range of solution schemes. In the present study, the Runge-Kutta third-order time scheme was employed and fifth- and third-order advection schemes were chosen for the horizontal and vertical directions, respectively (Skamarock et al., 2008). WRF/Chem simulates trace gas and particle chemical concentrations concurrently with the meteorological fields using the same grid structure, the same advection scheme, and the same physics schemes for sub-grid scale transport (Grell et al., 2005). The SOWC model was developed based on WRF/Chem V3.1.1 with significant modifications throughout the code to enable the use of 6D variables. The standard WRF/Chem model tracks 3-dimensionial chemistries in a 4-dimensional variable (X, Z, Y, Species). The SOWC model tracks a 6-dimensional chemical variable "AQC" (X, Z, Y, Size Bins, Source Types, Species). Particles emitted from different sources have different sizes and chemical compositions, leading

to a source-oriented mixture of particles that age in the atmosphere through coagulation and gas-particle conversion (e.g., condensation and evaporation) processes. Airborne particles in the SOWC model influence meteorological conditions through radiative feedbacks and microphysical processes. The model simultaneously tracks particle mass, number concentration, and radius. The number concentration and radius of different particle size bins from each source type are included as the last two elements in the species dimension. Simulations in this study use 38 chemical species (Table 1) from 5 emissions sources (wood smokes, gasoline, diesel, meat cooking, and other aerosol types) and 8 size bins. The initial particle sizes from emissions are 0.055, 0.1105, 0.221, 0.4415, 0.8835, 1.767, 3.535, and 7.0693 microns. Note that the SOWC model uses moving size bins whose sizes change in response to gas-particle conversion during model simulations. The model conserves aerosol mass concentration throughout the simulation of atmospheric processes including emissions, transport, deposition, coagulation, and condensation/evaporation. The gas-phase species emitted from different sources in each grid cell are not tracked separately in the SOWC model at the present time. In the current study, the initial and boundary conditions of aerosol particles are based on observations from the California Regional Particulate Air Quality Study (CRPAQS) (Ying et al., 2008). The distribution of particle emissions for different bins for every source are calculated using emissions inventories provided by the California Air Resources Board (CARB) along with measured chemical speciation profiles (Ying et al., 2008). Further details of the SOWC model structure and source-oriented chemistry processes are described by Zhang et al. (2014) and Joe et al. (2014).

2.2 Cloud microphysics scheme

The original Purdue Lin microphysics scheme was designed as a one-moment water mass conserved microphysics scheme with five hydrometeors: cloud water, rain, cloud ice, snow, and

graupel (Lin et al., 1983; Chen and Sun, 2002). Chapman et al. (2009) added a prognostic treatment of cloud droplet number (Ghan et al., 1997) to the Purdue Lin scheme to make a two-moment treatment of cloud water within WRF/Chem. In our study, a source-oriented CCN module was added to the SOWC model to track size-resolved information about activated CCN from various aerosol sources. A new source-oriented 6D cloud variable, "CLDAQC" (X, Z, Y, Size Bins, Source Types, Species) was added to SOWC to describe source-oriented clouds. Droplet radius and number concentration are once again stored as the last two elements in the species dimension of the CLDAQC variable. In the Purdue Lin scheme, all microphysics processes are parameterized with water mass, except autoconversion. Chapman et al. (2009) added the autoconversion parameterization from Liu et al. (2005) into the Purdue Lin microphysics, which depends on cloud droplet number. Chapman et al. (2009) also specified changes to cloud droplet number proportional to the microphysics process rate of cloud water mass. For example, when 10% cloud water becomes rain water after autoconversion, 10% cloud droplets will be moved at the same time.

The continuity equation of the mass-coupled mixing ratio of CLDAQC can be written as follows:

$$\frac{\partial CLDAQC}{\partial t} = \nabla \cdot \vec{V} CLDAQC + \nabla \cdot K \nabla CLDAQC + P_{AACT} + S_{micro}, \quad (1)$$

where $\vec{V}$ is the 3D wind vector and K is the eddy diffusion coefficient. The first two terms on the right hand side of Eq. (1) are the flux divergence of CLDAQC (transport) and sub-grid eddy mixing, respectively. Figure 1 shows the schematic diagram of the sinks and sources of CLDAQC in the cloud microphysics processes (P_{AACT} and S_{micro}). Aerosol activation (P_{AACT}) is the main source of CLDAQC. The calculation of aerosol activation is based on a maximum

supersaturation determined from a Gaussian spectrum of updraft velocities and aerosol chemistry composition for each size bin (Abdul-Razzak and Ghan, 2002). This parameterization of aerosol activation was implemented in WRF/Chem model (Chapman et al., 2009) and is used in this study. Aerosol activation was calculated each time step. Once the environment reached the critical supersaturation, AQC activated as CCN. Water vapor condenses at a diffusion limited rate to cloud droplets (water molecules transferred from vapor to cloud in Purdue Lin scheme) and particle mass/number is transferred from the interstitial aerosol variable (AQC) to the cloud-borne aerosol variable (CLDAQC). The Purdue Lin microphysics scheme uses a saturation adjustment approach (i.e., it adjusts water vapor to the saturation mixing ratio), so CCN activation is calculated before saturation adjustment. After saturation adjustment, the condensation rate due to vapor diffusion is proportional to particle size (Rogers and Yau, 1989). Results from CCN activation tests at relevant supersaturation are discussed in Section 4.3.

Sinks and sources of CLDAQC (S_{micro}) are based on interactions between a cloud droplet and the other hydrometeors (e.g., ice, rain, snow, and graupel) that can remove water from or add water to CLDAQC. The sinks of cloud water, as well as CLDAQC, include autoconversion from cloud to rain (P_{RAUT}) and the accretion of cloud water by rain (P_{RACW}), snow (P_{SACW}), and graupel (P_{GACW}). The exchange between cloud water and cloud ice can also occur through homogenous freezing of cloud water to ice (P_{IHOM}) and melting of cloud ice to cloud water (P_{IMLT}). Finally, the condensation (associated with P_{ACCT}) and evaporation of cloud water (P_{CEVP}) are implicitly taken into account in the Purdue Lin microphysics scheme. When cloud droplets fully evaporate (sink of CLDAQC), the residual cores are released back into the corresponding source type and size bin of the aerosol (AQC) variable.

232 **2.3 Radiation schemes**

233 The NASA Goddard shortwave and longwave radiation schemes (Chou and Suarez, 1999b,
234 2001b) are used in conjunction with the source-oriented cloud droplet algorithms in the enhanced
235 SOWC model. Absorption of radiation by water vapor, ozone, oxygen, carbon dioxide, cloud
236 droplets and aerosol particles is considered. Interactions among the absorption and scattering by
237 clouds and aerosols (Mie scattering), molecules (Rayleigh scattering) and the surface are fully
238 accounted for (Skamarock et al., 2008). Three main optical parameters are calculated for each
239 model layer to describe the influence of aerosols on the radiation: aerosol optical thickness (τ),
240 single scattering albedo (ω), and asymmetry factor (g). In the present study, the numerical code
241 described by Ying and Kleeman (2003) was implemented to calculate the optical properties of
242 source-oriented particles. The original numerical code of Mie scattering developed by Bohren
243 and Huffman (1983) was used to calculate the particle extinction efficiency, scattering efficiency
244 and asymmetry factor. The partial molar refractive index approach described in Stelson (1990)
245 was used to estimate the mean refractive index for multi-component aerosols. .

246 For any wavelength of shortwave or longwave radiation (λ), the aerosol optical thickness
247 (τ_a) of a model layer with depth h (m) containing a number concentration $n_a(r)$ (# m^{-3} μm^{-1}) of
248 droplets with radius r (μm) is given by

249 $$\tau_a(\lambda) = \pi h \int_0^\infty Q_e(\lambda, r) r^2 n_a(r)\, dr, \quad (2)$$

250 where, Q_e is the dimensionless extinction efficiency. The equivalent definition of aerosol optical
251 thickness for discrete size bins j with a mean radius r_j (μm) can be written as

252 $$\tau_a(\lambda) = \pi h \sum_i^n \sum_j^m Q_{ei,j}(\lambda, r) {r_{i,j}}^2 N_{i,j}, \quad (3)$$

where subscript *i* refers to emission source, subscript *j* refers to size, *n* is the number of particle source types and *m* is the number of particle sizes. N (# m^{-3}) is the number of particles. The mean asymmetry factor (g_a) and single scattering albedo (ω_a) are calculated using the method described in (Yang, 2000):

$$g_a(\lambda) = \frac{\sum_i^n \sum_j^m Q_{si,j}(\lambda,r) g_{i,j}(\lambda,r) N_{i,j} \pi r_{i,j}^2}{\sum_i^n \sum_j^m Q_{si,j}(\lambda,r) N_{i,j} \pi r_{i,j}^2}, \quad (4)$$

$$\omega_a(\lambda) = \frac{\sum_i^n \sum_j^m Q_{si,j}(\lambda,r) N_{i,j} \pi r_{i,j}^2}{\sum_i^n \sum_j^m Q_{ei,j}(\lambda,r) N_{i,j} \pi r_{i,j}^2}, \quad (5)$$

where Q_s is the dimensionless scattering efficiency. All of the optical parameters are functions of the wavelength (λ) of incident radiation.

In the original Goddard radiation schemes, cloud droplets are assigned to a mono-disperse size distribution (mean effective radius) which depends on the water mass and number concentration. The source-oriented cloud (CLDAQC) contains size distribution and chemistry information which is more realistic than the mono-disperse assumption. Equations 3-5 are applied to all size bins of not only the AQC but also the CLDAQC variables to calculate optical properties and radiative forcing.

3. Numerical experiment designs

3.1 Fog event

A numerical simulation of fog was carried out with the SOWC model to test the effects of particle mixing state on warm clouds processes. Fog is an excellent scientific case study that can isolate cloud activation and diffusive growth, the first step of aerosol-cloud-radiation interactions, from other microphysical processes that usually do not occur in fog, such as

collision/coalescence, riming, melting, and aggregation. This paper presents the development of the CLDAQC treatment within the SOWC model to ensure that the model performs properly. A careful selection of a weather phenomenon is important to evaluate the model performance and the impact of the aerosol mixture states on cloud formation. The involvement of other hydrometeors, in addition to cloud droplets, can not only change the cloud properties and cloud lifetime, but also modify the energy budget. These extremely nonlinear processes can significantly complicate the evaluation of the model performance and the first step of aerosol-cloud-radiation interaction. Thus we choose fog as our very first weather system study for the evaluation of aerosol-cloud-radiation interactions using the improved SOWC model. The influence of particle size and composition on fog formation and droplet growth has been studied in previous field experiments (Frank et al., 1998; Moore et al., 2004; Ming and Russell, 2004; Cubison et al., 2008; Niu et al., 2012) and modeling studies (Bott and Carmichael, 1993; Kleeman et al., 1997). The results indicate that particle chemical composition and mixing state strongly influence fog droplet activation, mirroring the processes of interest for cloud droplets. For example, the IPAC-NC field campaign in China observed clouds formed in a polluted environment with RH below 100% due to high hydroscopic pollutants (Ma et al., 2010).

Tule fogs (radiation fog) frequently form in the Central Valley of California during the winter season (Hayes et al., 1992). Winter in the Central Valley is associated with the maximum concentration of airborne particulate matter (PM) (Chow et al., 1993) which is composed of aerosol particles that can act as CCN. We chose Tule fog as our case study since it is important in safety, hydrology and agriculture in California and aerosols in California have been carefully investigated using the SOWC model (Joe et al., 2014; Zhang et al., 2014). In the present study, a thick fog event that occurred on 16 and 17 January 2011 (Fig. 2) was chosen to investigate the

296 impact of aging-process-included aerosol-cloud-radiation interactions on fog formation. Fog
297 started forming over the northern Central Valley on 13 January with observed surface relative
298 humidity reaching 95-100% and extended to the southern Central Valley on 14 January. The fog
299 became thicker on 16 January and reached the maximum on 17 January (Fig. 2). This is evident
300 by retrieved cloud optical thickness from MODIS (discussed later). The fog started dissipating
301 from the northern Central Valley on 18 January and fully dissipated on 19 January (Fig. 2c).
302 In addition to calm wind and radiative cooling, high moisture is an important ingredient to a
303 Tule fog event in the Central Valley, California. Figure 3 shows the time series of column
304 integrated water vapor, sea level pressure, and 850-hPa wind vectors from ECMWF Interim
305 reanalysis data. On 11 January, the column water vapor (CWV) was very low, less than 10 mm,
306 over the Central Valley (Fig. 3a). Moisture was advected into the Central Valley (Fig. 3b) by a
307 winter cyclone moving close to the northwestern coast of the United Sates on 12 January. A
308 weak southwest-northeast-oriented atmospheric river with a width of 1000 km and a maximum
309 CWV of ~26-28 mm approached the western coast and brought moisture into the Central Valley.
310 At 0000 UTC 13 January (Fig 3c), moisture content began increasing in the northern Central
311 Valley. At night, drainage flow from the surrounding mountains brought cold air into the
312 Central Valley, mixed with the low-level moist air, and initiated fog formation over the northern
313 Central Valley. On 14 January (Fig. 3d), the CWV over the southern Central Valley reached 22-
314 24 mm and fog formed over the southern Central Valley.
315 On 15 and 16 January, a more intense, west-southwest to east-northeast oriented
316 atmospheric river advected moisture into northern California (Figs. 3e and f). The moisture in
317 the Central Valley reached a maximum on 17 January (Fig. 3g), at the time when the fog reached
318 its maximum thickness during the study period (Fig. 2; also see the cloud optical thickness

discussion later). On 18 January (Fig. 3h), while high moisture and fog still presented over the southern Central Valley, the moisture decreased and the fog disappeared over the northern Central Valley. Fog fully dissipated in the Central Valley on 19 January.

According to the satellite images and surface temperature variation, the coverage and thickness of fog followed a diurnal pattern with thinning in the daytime and thickening at night. As mentioned earlier, the aerosol mixture state can impact fog formation and properties of cloud droplets.

3.2 Observational data

Multiple types of measurement data were used to evaluate the SOWC model performance. Moderate Resolution Imaging Spectroradiometer (MODIS) level 2 cloud products from the Terra and Aqua satellites provide 5-km resolution cloud optical thickness (COT) and liquid water path (LWP). The LWP retrieval from MODIS has been used to study low cloud and fog (Bendix et al., 2005). High-resolution MODIS data can describe fog spatial distribution and intensity but are only available once every 24 hours (daytime only) from each satellite. The SOWC model predictions for temperature and moisture at the surface are also evaluated against *in situ* time-series meteorological data from 24 surface weather stations along with net ground shortwave fluxes at 42 sites from California Irrigation Management Information System (CIMIS). Measured concentrations of airborne particles were obtained from the California Ambient Air Quality Data (CAAQD) provided by the Planning & Technical Support Division (PTSD) of the California Air Resources Board (CARB). The station details of CAAQD are provided in Table 2. The locations of all measurement sites are provided in Fig. 4.

3.3 Numerical experiment design

The primary objective of this study is to examine how the source-oriented (S_) (i.e., aging-process-included) and internal (I_) mixture representations of aerosol particles differ in their feedbacks to meteorology in a fog event. Internally mixed simulations (I_) artificially blend emissions from all sources into a single particle size distribution thereby concealing all advanced treatments of particle mixing and aging. Four experiments were carried out (Table 3) for the selected fog event. In the basecase experiment of S_ARon_CRmod, the polluted aerosol particles tracked by AQC act as the source of CCN (S_) and the aerosol-radiation interaction (aerosol direct effect) is enabled in the radiation schemes (ARon). The geometric-optics approach mentioned in Section 2.3 is used to calculate the cloud optical properties of each model layer (CRmod). S_ARon_CRorig is similar to S_ARon_CRmod, except for the use of the original cloud optical property calculation (CRorig) in the NASA Goddard shortwave and longwave radiation schemes. As discussed previously, the original schemes are based on an estimate of the cloud droplet effective radius using the cloud mass and number concentration (CRorig). The radius of cloud droplets in the original Goddard shortwave radiation scheme is constrained to the range from 4 μm to 20 μm. In the modified cloud-radiation scheme (CRmod), the size range of cloud droplets in Eq. (3) can vary between activated CCNs to 30 μm. S_ARoff_CRmod has no aerosol direct effect in the radiation schemes (ARoff). The comparison of S_ARoff_CRmod and S_ARon_CRmod is used to estimate the aerosol direct effect in this study.

Each numerical experiment employed two domains with two-way nesting. Domain 1 (86 x 97 grid cells) had a resolution of 12 km while domain 2 (127 x 202 grid cells) had a resolution of 4 km. Domain 2 was positioned to cover the entire Central Valley of California and results from

363 this domain are used for the subsequent analysis. All simulations used 31 vertically staggered
364 layers based on a terrain-following pressure coordinate system. The vertical layers are stretched
365 with a higher resolution near the surface (an average depth of ~30 m in the first model half
366 layer). Variables other than vertical velocity and geopotential were stored in the half model
367 levels. The time step was 60 seconds for the first domain and 20 seconds for the second domain.
368 The physics schemes employed for the simulations included the modified Purdue Lin
369 microphysics scheme (Chen and Sun, 2002), the NASA Goddard longwave/shortwave radiation
370 schemes (Chou and Suarez, 1999a, 2001a), the Kain-Fritsch cumulus scheme (Kain and Fritsch,
371 1990; Kain, 1993) (domain 1 only), the YSU PBL scheme (Hong et al., 2006; Hong, 2010) and
372 the Noah LSM surface scheme (Tewari et al., 2007). No cumulus scheme is used in the inner-
373 most domain (4 km resolution). The number of cloud droplets was not considered in the
374 convective scheme in the SOWC model. The target episode had calm winds with local fog
375 formation in the Central Valley (not propagating in through lateral boundaries). Moreover, the
376 event occurred in the winter season when the Convective Available Potential Energy (CAPE)
377 was small. Therefore, the KF cumulus convective parameterization is inactive for this cases
378 study. The meteorological initial and boundary conditions were taken from North American
379 Regional Reanalysis (NARR), which has a spatial resolution of 32 km and a temporal resolution
380 of 3 hours.

381 The SOWC model tracked two 6D variables for aerosol/cloud properties which introduce
382 considerable computational burden for model simulations when compared to standard
383 WRF/Chem model simulation (with prescribed aerosol concentration). The computational cost
384 of the SOWC model, which is proportional to the extra information that is tracked, is
385 approximately 25 times greater than the standard WRF/Chem 3.1.1 simulation with prescribed

aerosols (chem_opt = 0) or approximately 5 times greater than the standard WF/Chem 3.1.1 simulation with any chemistry option (/=0) in the current study. SOWC model simulations started at 0000 UTC 9 January (7 days prior to the start of the thick fog event) with four-dimensional data assimilation (FDDA), which nudges model fields in domain 1 to analysis including the u and v components of horizontal winds, water vapor mixing ratio, and temperature above the PBL height in all simulations. This approach provides a realistic heterogeneous aerosol distribution and low-level temperature and moisture fields at the start of the thick fog simulation. Observations from surface stations and NARR data were used for nudging during this aerosol spin-up period. Between 0000 UTC 16 January to 0000 UTC 19 January, the SOWC model integrated without FDDA (3 day free run) during which time the effects of the different model configurations were observed and is our major interested time period.

4. Model Results

4.1 Evaluation of basecase (S_ARon_CRmod) model performance

The SOWC model calculates CCN number concentrations based on the activation of aerosols (AQC). The AQC number concentration can influence the intensity of initial fog formation and spatial distribution of final fog fields, and thus AQC number concentration is examined first. Figure 5 shows 72-hour averaged (from 16 to 18 January 2011) AQC number concentrations in California's Central Valley that were also averaged over the first five model layers for S_ARon_CRmod. Fog usually forms within the planet boundary layer (PBL), which reaches to a height of approximately five model layers in winter conditions in the Central Valley (450-550 m). Temporally averaged AQC concentrations are approximately 2×10^{9} # m^{-3}, with the highest concentrations predicted in the vicinity of polluted cities (e.g., the San Francisco Bay Area, Stockton, Modesto, Sacramento, Fresno, and Bakersfield), in the middle of the Central

409 Valley, and at foothills of Sierra Nevada Mountain over the east-southeastern Central Valley.

410 Figure 6 shows the comparison of simulated nitrate (NO_3^-), sulfate (SO_4^{2-}), ammonium
411 (NH_4^+) and soluble sodium (Na^+) concentrations to measured values at 6 monitoring stations (see
412 Table 2 and Fig. 4) on 18 January 2011. Simulated sulfate and soluble sodium are in reasonable
413 (>80%) agreement with measurements but nitrate and ammonium concentrations were under
414 predicted by approximately 70%. The cause for this discrepancy is unknown, but one possibility
415 is that after fog dissipates on 18 January, most Ammonium and Nitrate are released back to the
416 gas phase. This potentially explains why Nitrate and Ammonium are significantly
417 underestimated in the condensed phase (Fig. 6). Unfortunately, we only have observations on
418 the last day of the simulation (18 January) when fog almost dissipated. With this limited
419 observations, it is difficult to effectively evaluate the cause of the underestimation of Nitrate and
420 Ammonium. Note that both observed and predicted nitrate concentrations in the current episode
421 are lower than the maximum concentrations observed in historical extreme episodes within the
422 San Joaquin Valley (SJV) because the current stagnation event only lasted a few days while
423 extreme events last multiple weeks. If more discussion of aerosol perditions form the SOWC
424 model is desired, we refer the reader to Zhang et al. (2014) who present a comparison of
425 predicted aerosol concentrations and measured concentrations using field campaign data
426 measured during the California Regional PM_{10} / $PM_{2.5}$ Air Quality Study (CRPAQS) in
427 December 2000 – January 2001.

428 The S_ARon_CRmod experiment reasonably reproduces the observed spatial distribution
429 and magnitude of liquid water path (LWP) compared to the data retrieved from MODIS (Fig. 7).
430 In particular, the model predicts LWP well over the northern portion of the Central Valley during
431 the fog event (16 to 18 January). However, the model under-predicts LWP in the middle portion

of the Central Valley, which caused the fog to dissipate earlier (late 17 January). Once the surface temperature increases in one area due to thin fog, the dissipation spreads out quickly until the fog completely evaporates. For the southern portion of the Central Valley, the fog event starts earlier (14 to 15 January) and the model reasonably predicts the onset of the event. But the simulated fog is too dense (figure not shown). In addition, the peak of the simulated fog occurs one day earlier (16 January forecast versus 17 January observed). This timing difference could be caused by the change in the microphysics processes at 0000 UTC 16 January. During the FDDA time period (before 16 January), the one-moment bulk microphysics scheme is used. After the FDDA time period, aerosols start being involved in cloud formation. High Nitrate concentrates in the SJV and enhances aerosol activation due to its high hygroscopicity. This could partially explain why the peak of the LWP occurs on 16 January. The details of aerosol chemical properties are discussed by Zhang et al. (2014).

While simulated LWP is comparable to MODIS retrievals with one-day shift (Fig. 7), to obtain a higher COT than observed (Fig. 8b versus 8c) we expect that the model produces more small cloud droplets with a higher CCN concentration, especially over highly polluted areas. High predicted COT results in cold surface temperature, especially in the southern portion of the Central Valley. Overall, the spatial distribution and magnitude of simulated COT also match the satellite data reasonably (Fig. 8), except for the overestimation of COT over the southeastern Central Valley (Fig. 8b and d).

Mean biases of 2-m temperature (T2), 2-m water vapor mixing ratio (Q2), and surface net downward shortwave radiative flux (NSF) over the entire Central Valley from 16 to 18 January 2011 for S_ARon_CRmod are calculated (Fig. 9). Generally, T2 and Q2 of S_ARon_CRmod are under-predicted by 2 °C and 0.7 g kg^{-1}, respectively. The predicted time variation of T2 and Q2

biases is small in the first one and half days but increases after 1600 UTC 17 January because the predicted fog dissipated in the daytime, different from observations. Since the predicted fog dissipated, simulated NSF increased and was over-predicted by 13.9 W m^{-2}. Low simulated T2 and Q2, particularly during first one and half days, in S_ARon_CRmod are partially due to over-predictions of the fog formation (i.e., too much condensation leading to depleted water vapor), especially over the southern portion of the Central Valley. Overall, S_ARon_CRmod reasonably forecasted LWP and COT spatial pattern and intensity. S_ARon_CRmod also captured the diurnal pattern of T2 and Q2 during the fog event, but under-predicted the absolute magnitude of T2 and Q2 by 1.76 (2.22) °C and 0.56 (0.88) g kg^{-1} in the daytime (nighttime), respectively.

4.2 Source-oriented aerosol direct and indirect effects

S_ARoff_CRmod is designed to test aerosol-radiation feedback and so the comparison between S_ARoff_CRmod and S_ARon_CRmod can help quantify the aerosol direct effect in the current study. Table 4 shows that the hourly bias mean and standard deviation from 24 surface stations in the daytime and nighttime of S_ARoff_CRmod are similar to, but larger than, results from S_ARon_CRmod for T2 and Q2 at the ground. However, compared to S_ARon_CRmod, the smaller cold bias from S_ARoff_CRmod is consistent with its larger net downward shortwave radiative flux (NSF) shown in Tables 4 and 5. Table 5 shows that the average NSF within the entire Central Valley from S_ARoff_CRmod is higher than S_ARon_CRmod by 3.7 W m^{-2}, which means that the shortwave energy flux that reached the ground was reduced by ~3.7 W m^{-2} due to aerosol radiative forcing in this case study. The maximum increases of T2 and NSF by the aerosol direct effect occurred on 17 January 2011 (Fig. 9). Table 5 also shows the mean value of cloud liquid water, cloud droplet number, surface skin temperature, latent heat flux and sensible heat flux over the Central Valley during 16 to 18

January 2011. Cloud liquid water and cloud droplet number were averaged within the first five model layers. The aerosol direct effect leads to increases in the cloud water mass and cloud droplet number by 3.3% and 4.5%, respectively, due to reductions in skin temperature (0.1 K) and net shortwave flux (3.7 W m^{-2}).

The modified radiation schemes for cloud optical properties in the S_ARon_CRmod experiment do not have significant feedback on spatially and temporally averaged cloud water mass (i.e., compared to S_ARon_CRorig) as shown in Table 5. However, the modified cloud-radiation interaction (i.e., geometric-optics method) used in the COT calculations (S_ARon_CRmod) predicts slightly higher COT, which leads to slightly lower net shortwave flux and surface skin temperature, especially in the polluted area. The higher COT predictions are likely caused by differences in the size range of cloud droplets and refractive indexes of cloud water with/without chemical composition in the calculation of cloud radiative properties. In the original radiation scheme, the cloud optical thickness (COT) is a function of cloud water path (CWP) and an effective radius (4 μm ≤ r_e ≤ 20 μm), which is derived from the water mass and the total droplet number assuming a uniform size of cloud droplets:

$$\tau_{orig}(\lambda) = CWP \times (-6.59\times10^{-3} + \frac{1.65}{r_e}). \quad (6)$$

In the modified radiation scheme in S_ARon_CRmod, the COT is calculated based on simulated cloud droplet size, number, and chemical composition of each bin and source (Eq. 3). In addition, the formula of COT, single scattering albedo and asymmetry factor in the modified radiation scheme are all modified. With a similar Q_c, although Q_n in S_ARon_CRorig is higher than that in S_ARon_CRmod, the COT is slightly higher in S_ARon_CRmod due to different formulas used in the calculation of cloud-radiation interaction. The small difference of COT

between these two experiments in fact indicates that the parameterization of COT in the original radiation scheme provides a reasonable result compared to the explicit COT calculation.

Because the meteorological conditions of the fog event are calm and stable, the cloud microphysics processes are fairly slow and simple (no rain produced in this case). Although S_ARon_CRorig had slightly higher cloud droplet number concentrations, the modified calculation of the cloud optical properties in S_ARon_CRmod gave a similar cloud amount and net shortwave radiation flux reaching the surface, which produced nearly identical feedbacks to meteorology in both experiments (Table 5).

4.3 Internal mixture versus source-oriented aerosols

The mixing state of chemical components among the atmospheric aerosol particles can potentially play an important role in fog formation. The activation of aerosol particles into cloud droplets depends on the critical supersaturation which in turn depends on particle composition. According to the Köhler equation, increased concentrations of solutes will decrease the critical supersaturation required to activate a particle into a CCN. As mentioned earlier, hydrophobic particles (i.e. black carbon) will more easily serve as CCN once they are coated with hygroscopic material (i.e. sulfate). Increased concentrations of solutes can potentially modify the frequency and severity of fog events in polluted air. In this section, we compare results from S_ARon_CRmod (source-oriented (i.e., aging-process-included) experiment) and I_ARon_CRmod (internally mixed experiment) to investigate the activation change and further meteorological responses between internally mixed and source-oriented aerosols. The internally mixed experiment is conducted by lumping all sources together (i.e., AQC source dimension collapsed to one producing a 5D AQC variable).

522 It is likely that the ratio of CCN concentration (N_{CCN}) to total aerosol concentration (N_{CN})
523 will be different for each of the five source types tracked in S_ARon_CRmod since the CCN
524 activation depends on the chemical composition and size of the particles. The highest ratio of
525 N_{CCN}/N_{CN} for S_ARon_CRmod and I_ARon_CRmod is located in the southern Central Valley
526 (Fig. 10) due to higher moisture from the atmospheric river resulting in greater aerosols
527 activation to CCNs and smaller residual aerosol number concentration (see Fig. 5). Over the
528 Central Valley during 16 to 18 January 2011, the ratio of N_{CCN}/N_{CN} for each source type is
529 12.63%, 15.60%, 14.89%, 16.80% and 20.21% for wood smoke, gasoline, diesel, meat cooking,
530 and others, respectively (averaged within the first five model layers). Wood smoke is typically a
531 major source of aerosol (~38%) in California's Central Valley during winter stagnation events
532 (see Table 6) and the organic carbon in wood smoke is water-soluble (Dusek et al., 2011) which
533 allows these particles to activate more easily than insoluble particles. However, the majority of
534 the wood smoke particles are located in the smallest size bin, so the ratio of N_{CCN}/N_{CN} for wood
535 smoke is comparable with that of hydrophobic diesel. The source type of "others", which has the
536 highest ratio of N_{CCN}/N_{CN}, is dominated by larger dust particles coated with secondary
537 components such as nitrate and are easier to activate, in contrast to the smaller combustion
538 particles emitted from other tracked sources.
539 The comparison of the average ratio of N_{CCN}/N_{CN} from the first five model layers between
540 S_ARon_CRmod and I_ARon_CRmod is shown on Fig. 10. The spatial patterns produced by
541 both experiments are similar but I_ARon_CRmod has a higher N_{CCN}/N_{CN} ratio, in particular over
542 the northern two thirds of the Central Valley. The largest differences between N_{CCN}/N_{CN}
543 predicted by S_ARon_CRmod and I_ARon_CRmod occur in regions with large emissions of
544 wood smoke (figure not shown). The ratio of N_{CCN}/N_{CN} for both experiments can reach >30%

but the highest N_{CCN}/N_{CN} ratio occurs in relatively less polluted regions. The spatially averaged ratio of N_{CCN}/N_{CN} is 16.65% for S_ARon_CRmod and 27.49% for I_ARon_CRmod within the Central Valley over the period of 16 to 18 January. The CCN concentrations and N_{CCN}/N_{CN} ratios between internally mixed and source-oriented experiments at different supersaturations were calculated to better understand this result. Figure 11a shows the 72-hour averaged CCN concentration at supersaturations of 0.02%, 0.05%, 0.1%, 0.2% and 0.5% and total AQC concentration averaged within the first five model layers. Figure 11b presents corresponding N_{CCN}/N_{CN} ratios at 5 different supersaturations. When the supersaturation is less than or equal to 0.2%, the N_{CCN}/N_{CN} ratio predicted from S_ARon_CRmod is comparable or even slightly higher than that predicted from I_ARon_CRmod. In the S_ARon_CRmod tests, 56% of the particles tracked in the AQC variable (mainly in size bins 2-8) are activated as CCN. When the supersaturation is close to 0.5%, the N_{CCN}/N_{CN} ratio from I_ARon_CRmod can be 15% higher than that of S_ARon_CRmod. Most particles tracked in the AQC size bin 1 can activate in the internally mixed experiment; however, in the source-oriented experiment only particles emitted in AQC size bin 1 from wood smoke and "others sources" are sufficiently hygroscopic to activate. The remaining sources are dominated by hydrophobic compounds (such as elemental carbon) that do not activate under the study conditions (Table 6). Cubison et al. (2008) analyzed observational CCN and CN data in 2005 from a field campaign in California and found that the average ratio of N_{CCN}/N_{CN} was 18% for a supersaturation value of 0.5%, but their predicted N_{CCN}/N_{CN} ratio based on the internal mixture assumptions could reach to more than 50%. In the source-oriented SOWC model, supersaturation values are typically ~0.2-0.3% with maximum value of 0.5% in some areas. The estimated ratio of N_{CCN}/N_{CN} in the source-oriented model is comparable with observations in Cubison et al. (2008), especially in polluted areas. The temporal

568 variations of mean bias of 2-m temperature (T2), 2-m water vapor mixing ratio (Q2), and surface
569 net downward shortwave radiative flux (NSF) between internal versus external aerosol mixture
570 states (I_ARon_CRmod versus S_ARon_CRmod) are similar until 2000 UTC 17 January. After
571 late 17 January, the bias differences between two experiments are more apparent in the daytime
572 than in the nighttime (Fig. 9 and Table 4). Compared to I_ARon_CRmod, S_ARon_CRmod
573 reduced bias in T2 by 0.25 K in the daytime but had higher bias in NSF. S_ARon_CRmod did
574 predict improved values of Q2. Based on Fig. 9, we know that the source-oriented and internal
575 aerosol mixing states mainly cause differences in surface temperature in the daytime. Figures
576 12a and b illustrate the relative change ((internally mixed – source-oriented)/source-oriented *
577 100%) of averaged (16 - 18 January 2011) cloud liquid water and cloud droplet number,
578 respectively, during the daytime. I_ARon_CRmod predicts cloud liquid water that are 40%
579 higher than values predicted by S_ARon_CRmod over the northern Central Valley (Fig. 12a).
580 The largest relative change in predicted cloud water concentration also occurs in the northern
581 Central Valley near the mountains where fogs are initiated by drainage flow. I_ARon_CRmod
582 predicts higher cloud droplet number (Fig. 12b), with the largest relative increases (50~60%)
583 once again observed in areas near mountains and highly polluted regions with more modest
584 changes of 20~30% over remote regions. Internally mixed aerosols reduce the critical saturation
585 ratio for particles by artificially mixing hygroscopic and hydrophobic components that in turn
586 allows particles to activate more easily.

587 The internally mixed experiment (I_ARon_CRmod) predicts lower daytime averaged
588 surface skin temperature and net downward shortwave flux at ground (Fig. 12c and d)
589 corresponding to the areas with higher cloud liquid water and cloud droplet concentrations (Fig.
590 12a and b). This result is expected since higher cloud liquid water and cloud droplet

591 concentration will reduce the solar radiation flux on the surface. The reduction of surface skin
592 temperature in the internal mixed experiment is proportional to the change of the net shortwave
593 radiation. Figure 13 shows that the area average of latent heat flux (LH) and sensible heat flux
594 (SH) over the Central Valley in S_ARon_CRmod and the average difference of internally mixed
595 and source-oriented experiments. Higher cloud amount and lower surface temperature are
596 predicted in the internally mixed experiment leading to reduced LH and SH fluxes at ground
597 level compared to the source-oriented experiment. The difference between internally mixed and
598 source-oriented predictions for LH and SH reached 3 W m^{-2} and 5 W m^{-2}, respectively, at noon
599 local time (2200 UTC 17 January).

600 Table 7 shows hourly mean bias and root-mean-square-difference between internally mixed
601 (I_ARon_CRmod) and source-oriented (S_ARon_CRmod) experiments for six variables within
602 the Central Valley during 16 to 18 January 2011. The mean bias between these two experiments
603 is 1.19×10^{-2} (g m^{-3}) for cloud liquid water and 6.24×10^{7} (# m^{-3}) for cloud droplet number. The
604 direction of these trends is expected since internally mixed aerosols are easier to activate as
605 CCN. The mean bias between internally mixed and source-oriented experiments is -0.15 (K) for
606 surface skin temperature and -6.02 (W m^{-2}) for net shortwave flux. The mean bias of LH and SH
607 is -0.61 and -0.36 (W m^{-2}), respectively. The root-mean-square-difference between these two
608 experiments is large for each variable, meaning that the difference varies strongly with location
609 (see Fig. 12).

610 In summary, compared to S_ARon_CRmod, I_ARon_CRmod has a higher CCN / cloud
611 droplet number concentration because internally mixed aerosols can instantaneously contain
612 hydroscopic material (e.g. sulfate) through artificial mixing, which decreases the critical
613 supersaturation requirement for a particle to activate into a CCN, leading to higher cloud number

614 concentration and optical thickness. Thicker fog in I_ARon_CRmod reduces the amount of
615 shortwave radiation reaching the surface, resulting in a lower surface temperature. A lower
616 surface temperature can have a positive feedback on cloud lifetime (i.e., a longer cloud lifetime),
617 which further reduces shortwave radiation reaching the surface when compared to
618 S_ARon_CRmod. Hence, the aerosols that include aging processes can delay CCN activation
619 and produce fewer cloud droplets and less fog, which in turn will modify the energy budget near
620 the surface.

621 **5. Summary and discussion**

622 A warm cloud-aerosol interaction module was implemented into the source-oriented
623 Weather Research and Forecasting model with Chemistry (SOWC) to study the aerosol-cloud-
624 radiation interactions during fog simulations. The source-oriented mixture of aerosols is used to
625 explicitly simulate particle aging processes in the atmosphere rather than instantaneously
626 combining particles into an internal mixture. The SOWC model was used to simulate a fog
627 event in California's Central Valley in January 2011 with seven days of FDDA nudging and
628 three days of free run. Fog formation occurred when high moisture content from an Atmospheric
629 River was advected into the Central Valley and cold drainage flows occurred into the valley at
630 night. The initial tests used 5 emissions sources (wood smoke, gasoline, diesel, meat cooking,
631 and others) with particles from each source consisting of 38 chemical species and 8 size bins,
632 spanning a diameter range from 0.01 to 10 microns. The highest model spatial resolution was 4
633 km.

634 Four numerical experiments were conducted to test model performance, meteorological
635 feedbacks from internal and source-oriented aerosols, and the impact of aerosol-cloud-radiation
636 interaction on fog formation. Compared to observations, the SOWC model reasonably predicted

637 fog spatial distribution and duration and environmental meteorological feedbacks. However, the
638 model over-predicted liquid water path and cloud optical thickness, which resulted in cold
639 surface temperature bias. The inclusion of aerosol-radiation interaction reduced net downward
640 shortwave radiative flux by an average of 3.7 W m^{-2} and daytime surface temperature by 0.1 K.
641 Results that used different treatments for aerosol mixing states were compared, and the important
642 results are: 1) the fraction of N_{CCN}/N_{CN} at a supersaturation of 0.5% in the Central Valley
643 decreased from 94% in the internal mixture model to 80% in the source-oriented mixture model;
644 2) due to a smaller number of the CCN concentration in the source-oriented mixture model than
645 in the internal mixture model, cloud liquid water and cloud droplet number decreased 5% and
646 15%, respectively; and 3) compared to observations, the source-oriented mixture model reduced
647 the cold bias for surface temperature by 0.25 K in the daytime relative to the internal mixture
648 model. The source-oriented mixture representation of particles also provided more reasonable
649 predictions for cloud droplet number and cloud water mass versus observations due to different
650 activation properties than the internal mixture representation of particles. The internal mixture
651 model predicted greater activation of CCN than the source-oriented model due to artificial
652 coating of hydrophobic particles with hygroscopic components.
653 The SOWC model in this study explicitly calculates primary particle aging over a regional
654 scale for fog formation prediction with two-moment microphysics scheme and aerosol-cloud-
655 radiation interactions. The SOWC model should be a useful tool to study aerosol-cloud-radiation
656 interactions. Note that the current results are based on a Tule fog case study in the Central
657 Valley of California. Additional fog case studies under different weather conditions in other
658 regions of the world are required to draw conclusions at those locations.
659

Acknowledgment

The authors thank two anonymous reviewers for their insightful comments on the manuscript. The authors would also like to thank the WRF and WRF/Chem teams for their efforts on model development. This study was funded by the United States Environmental Protection Agency under Grant No. R833372, NASA Grant No. NNX09AC38G, and NASA High-End Computing (HEC) Program through the NASA Advanced Supercomputing (NAS) Division at Ames Research Center (SMD-13-3895). Although the research described in the article has been funded by the United States Environmental Protection Agency it has not been subject to the Agency's required peer and policy review and therefore does not necessarily reflect the reviews of the Agency and no official endorsement should be inferred.

References

Abdul-Razzak, H., and Ghan, S. J.: A parameterization of aerosol activation 3. Sectional representation, Journal of Geophysical Research: Atmospheres, 107, AAC 1-1-AAC 1-6, 10.1029/2001jd000483, 2002.

Ackerman, A. S., Toon, O. B., Stevens, D. E., Heymsfield, A. J., Ramanathan, V., and Welton, E. J.: Reduction of Tropical Cloudiness by Soot, Science, 288, 1042-1047, 10.1126/science.288.5468.1042, 2000.

Ackermann, I. J., Hass, H., Memmesheimer, M., Ebel, A., Binkowski, F. S., and Shankar, U.: Modal aerosol dynamics model for Europe: development and first applications, Atmospheric Environment, 32, 2981-2999, http://dx.doi.org/10.1016/S1352-2310(98)00006-5, 1998.

Adams, P. J., Seinfeld, J. H., Koch, D., Mickley, L., and Jacob, D.: General circulation model assessment of direct radiative forcing by the sulfate-nitrate-ammonium-water inorganic aerosol system, Journal of Geophysical Research-Atmospheres, 106, 1097-1111, 10.1029/2000jd900512, 2001.

Albrecht, B. A.: AEROSOLS, CLOUD MICROPHYSICS, AND FRACTIONAL CLOUDINESS, Science, 245, 1227-1230, 10.1126/science.245.4923.1227, 1989.

Anttila, T.: Sensitivity of cloud droplet formation to the numerical treatment of the particle mixing state, Journal of Geophysical Research: Atmospheres, 115, n/a-n/a, 10.1029/2010JD013995, 2010.

Bendix, J., Thies, B., Cermak, J., and Nau\ss, T.: Ground fog detection from space based on MODIS daytime data-a feasibility study, Weather and forecasting, 20, 989-1005, 2005.

693 Binkowski, F. S., and Shankar, U.: The Regional Particulate Matter Model: 1. Model
694 description and preliminary results, Journal of Geophysical Research: Atmospheres, 100,
695 26191-26209, 10.1029/95jd02093, 1995.
696 Bohren, C. F., and Huffman, D. R.: Absorption and Scattering of Light by Small Particles,
697 Wiley, New York., 1983.
698 Bott, A., and Carmichael, G. R.: Multiphase chemistry in a microphysical radiation fog
699 model—A numerical study, Atmospheric Environment. Part A. General Topics, 27, 503-522,
700 http://dx.doi.org/10.1016/0960-1686(93)90208-G, 1993.
701 Chapman, E. G., Gustafson Jr, W. I., Easter, R. C., Barnard, J. C., Ghan, S. J., Pekour, M. S., and
702 Fast, J. D.: Coupling aerosol-cloud-radiative processes in the WRF-Chem model:
703 Investigating the radiative impact of elevated point sources, Atmos. Chem. Phys., 9, 945-
704 964, 10.5194/acp-9-945-2009, 2009.
705 Chen, J.-P., and Lamb, D.: Simulation of Cloud Microphysical and Chemical Processes Using a
706 Multicomponent Framework. Part I: Description of the Microphysical Model, Journal of the
707 Atmospheric Sciences, 51, 2613-2630, 1994.
708 Chen, J.-P., Hazra, A., Shiu, C.-J., Tsai, I.-C., and Lee, H.-H.: Interaction between Aerosols and
709 Clouds: Current Understanding, in: Recent Progress in Atmospheric Sciences: Applicatons
710 to the Asia-Pacific Region, edited by: Liou, K. N., and Chou, M.-D., World Scientific
711 Publishing Co. Pte. Ltd., 231-281, 2008.
712 Chen, S.-H., and Sun, W. Y.: A one-dimensional time-dependent cloud model, j. Meteor. Soc.
713 Japan, 80, 99-118, 2002.
714 Chou, M.-D., and Suarez, M. J.: A Solar Radiation Parameterization for Atmospheric Studies
715 NASA Tech. Rep. NASA/TM-1999-10460, 15, 1999a.
716 Chou, M.-D., and Suarez, M. J.: A Thermal Infrared Radiation Parameterization for
717 Atmospheric Studies, NASA Tech. Rep. NASA/TM-2001-104606, 19, 2001a.
718 Chou, M. D., and Suarez, M. J.: A solar radiation parameterization for atmospheric studies.,
719 NASA Tech. Rep., 38, 1999b.
720 Chou, M. D., and Suarez, M. J.: A thermal infrared radiation parameterization for
721 atmospheric studies. , NASA Tech. Rep., 55, 2001b.
722 Chow, J. C., Watson, J. G., Lowenthal, D. H., Solomon, P. A., Magliano, K. L., Ziman, S. D., and
723 Richards, L. W.: PM10 and PM2.5 Compositions in California's San Joaquin Valley, Aerosol
724 Science and Technology, 18, 105-128, 10.1080/02786829308959588, 1993.
725 Cubison, M. J., Ervens, B., Feingold, G., Docherty, K. S., Ulbrich, I. M., Shields, L., Prather, K.,
726 Hering, S., and Jimenez, J. L.: The influence of chemical composition and mixing state of Los
727 Angeles urban aerosol on CCN number and cloud properties, Atmos. Chem. Phys., 8, 5649-
728 5667, 10.5194/acp-8-5649-2008, 2008.
729 Dick, W. D., Saxena, P., and McMurry, P. H.: Estimation of water uptake by organic
730 compounds in submicron aerosols measured during the Southeastern Aerosol and
731 Visibility Study, Journal of Geophysical Research: Atmospheres (1984–2012), 105, 1471-
732 1479, 2000.
733 Dusek, U., Reischl, G. P., and Hitzenberger, R.: CCN Activation of Pure and Coated Carbon
734 Black Particles, Environmental Science & Technology, 40, 1223-1230, 10.1021/es0503478,
735 2006.
736 Dusek, U., Frank, G. P., Massling, A., Zeromskiene, K., Iinuma, Y., Schmid, O., Helas, G.,
737 Hennig, T., Wiedensohler, A., and Andreae, M. O.: Water uptake by biomass burning aerosol

738 at sub- and supersaturated conditions: closure studies and implications for the role of
739 organics, Atmos. Chem. Phys., 11, 9519-9532, 10.5194/acp-11-9519-2011, 2011.
740 Fast, J. D., Gustafson, W. I., Easter, R. C., Zaveri, R. A., Barnard, J. C., Chapman, E. G., Grell, G.
741 A., and Peckham, S. E.: Evolution of ozone, particulates, and aerosol direct radiative forcing
742 in the vicinity of Houston using a fully coupled meteorology-chemistry-aerosol model,
743 Journal of Geophysical Research: Atmospheres, 111, D21305, 10.1029/2005jd006721,
744 2006.
745 Frank, G., Martinsson, B. G., Cederfelt, S.-I., Berg, O. H., Swietlicki, E., Wendisch, M.,
746 Yuskiewicz, B., Heintzenberg, J., Wiedensohler, A., Orsini, D., Stratmann, F., Laj, P., and Ricci,
747 L.: Droplet Formation and Growth in Polluted Fogs, Contri. Atmos. Phys., 71, 65-85, 1998.
748 Georgii, H. W., and Kleinjung, E.: Relations between the chemical composition of
749 atmospheric aerosol particles and the concentration of natural ice nuclei. , J. Rech. Atmos.,
750 3, 145-156, 1967.
751 Ghan, S. J., Leung, L. R., Easter, R. C., and Abdul-Razzak, H.: Prediction of cloud droplet
752 number in a general circulation model, Journal of Geophysical Research: Atmospheres, 102,
753 21777-21794, 10.1029/97jd01810, 1997.
754 Grell, G. A., Peckham, S. E., Schmitz, R., McKeen, S. A., Frost, G., Skamarock, W. C., and Eder,
755 B.: Fully coupled "online" chemistry within the WRF model, Atmospheric Environment, 39,
756 6957-6975, http://dx.doi.org/10.1016/j.atmosenv.2005.04.027, 2005.
757 Griffin, D. W., Kellogg, C. A., and Shinn, E. A.: Dust in the wind: Long range transport of dust
758 in the atmosphere and its implications for global public and ecosystem health, Global
759 Change and Human Health, 2, 20-33, 2001.
760 Hayes, T. P., Kinney, J. J. R., and Wheeler, N. J. M.: California surface wind climatology,
761 California Air Resources Board, Technical Support Division, Modeling and Meteorology
762 Branch, 1992.
763 Hong, S.-Y., Noh, Y., and Dudhia, J.: A New Vertical Diffusion Package with an Explicit
764 Treatment of Entrainment Processes, Monthly Weather Review, 134, 2318-2341,
765 10.1175/mwr3199.1, 2006.
766 Hong, S.-Y.: A new stable boundary-layer mixing scheme and its impact on the simulated
767 East Asian summer monsoon, Quarterly Journal of the Royal Meteorological Society, 136,
768 1481-1496, 10.1002/qj.665, 2010.
769 IPCC: Climate change 2007-the physical science basis: Working group I contribution to the
770 fourth assessment report of the IPCC, Cambridge University Press, 2007.
771 Joe, D. K., Zhang, H., DeNero, S. P., Lee, H.-H., Chen, S.-H., McDonald, B. C., Harley, R. A., and
772 Kleeman, M. J.: Implementation of a high-resolution Source-Oriented WRF/Chem model at
773 the Port of Oakland, Atmospheric Environment, 82, 351-363,
774 http://dx.doi.org/10.1016/j.atmosenv.2013.09.055, 2014.
775 Kain, J. S., and Fritsch, J. M.: A one-dimensional entraining/detraining plume model and its
776 application in convective parameterization, Journal of the atmospheric sciences, 47, 2784-
777 2802, 1990.
778 Kain, J. S.: Convective parameterization for mesoscale models: The Kain-Fritsch scheme,
779 The representation of cumulus convection in numerical models, Meteor. Monogr, 46, 165-
780 170, 1993.
781 Kleeman, M. J., Cass, G. R., and Eldering, A.: Modeling the airborne particle complex as a
782 source-oriented external mixture, Journal of Geophysical Research-Atmospheres, 102,
783 21355-21372, 10.1029/97jd01261, 1997.

784 Koch, D., and Del Genio, A. D.: Black carbon semi-direct effects on cloud cover: review and
785 synthesis, Atmos. Chem. Phys., 10, 7685-7696, 10.5194/acp-10-7685-2010, 2010.
786 Lance, S., Raatikainen, T., Onasch, T. B., Worsnop, D. R., Yu, X. Y., Alexander, M. L.,
787 Stolzenburg, M. R., McMurry, P. H., Smith, J. N., and Nenes, A.: Aerosol mixing state,
788 hygroscopic growth and cloud activation efficiency during MIRAGE 2006, Atmos. Chem.
789 Phys., 13, 5049-5062, 10.5194/acp-13-5049-2013, 2013.
790 Lesins, G., Chylek, P., and Lohmann, U.: A study of internal and external mixing scenarios
791 and its effect on aerosol optical properties and direct radiative forcing, Journal of
792 Geophysical Research-Atmospheres, 107, 10.1029/2001jd000973, 2002.
793 Li, W. J., and Shao, L. Y.: Observation of nitrate coatings on atmospheric mineral dust
794 particles, Atmos. Chem. Phys., 9, 1863-1871, 10.5194/acp-9-1863-2009, 2009.
795 Lin, Y.-L., Farley, R. D., and Orville, H. D.: Bulk Parameterization of the Snow Field in a Cloud
796 Model, Journal of Climate and Applied Meteorology, 22, 1065-1092, 1983.
797 Liu, Y., Daum, P. H., and McGraw, R. L.: Size truncation effect, threshold behavior, and a new
798 type of autoconversion parameterization, Geophysical Research Letters, 32, L11811,
799 10.1029/2005gl022636, 2005.
800 Lohmann, U., and Feichter, J.: Global indirect aerosol effects: a review, Atmos. Chem. Phys.,
801 5, 715-737, 10.5194/acp-5-715-2005, 2005.
802 Ma, J., Chen, Y., Wang, W., Yan, P., Liu, H., Yang, S., Hu, Z., and Lelieveld, J.: Strong air
803 pollution causes widespread haze-clouds over China, Journal of Geophysical Research:
804 Atmospheres, 115, n/a-n/a, 10.1029/2009JD013065, 2010.
805 McMichael, A. J., Woodruff, R. E., and Hales, S.: Climate change and human health: present
806 and future risks, The Lancet, 367, 859-869, 2006.
807 Ming, Y., and Russell, L. M.: Organic aerosol effects on fog droplet spectra, Journal of
808 Geophysical Research: Atmospheres, 109, D10206, 10.1029/2003jd004427, 2004.
809 Moore, K. F., Sherman, D. E., Reilly, J. E., and Collett, J. L.: Drop size-dependent chemical
810 composition in clouds and fogs. Part I. Observations, Atmospheric Environment, 38, 1389-
811 1402, http://dx.doi.org/10.1016/j.atmosenv.2003.12.013, 2004.
812 Motoi, K.: Electron-microscope study of snow crystal nuclei, Journal of Meterology, 8, 151-
813 156, 1951.
814 Niu, S. J., Liu, D. Y., Zhao, L. J., Lu, C. S., Lü, J. J., and Yang, J.: Summary of a 4-Year Fog Field
815 Study in Northern Nanjing, Part 2: Fog Microphysics, Pure and Applied Geophysics, 169,
816 1137-1155, 10.1007/s00024-011-0344-9, 2012.
817 Ramanathan, V., Crutzen, P. J., Kiehl, J. T., and Rosenfeld, D.: Atmosphere - Aerosols, climate,
818 and the hydrological cycle, Science, 294, 2119-2124, 10.1126/science.1064034, 2001.
819 Rogers, R. R., and Yau, M. K.: A Short Course in Cloud Physics, Third ed., Butterworth
820 Heinemann, 1989.
821 Schell, B., Ackermann, I. J., Hass, H., Binkowski, F. S., and Ebel, A.: Modeling the formation of
822 secondary organic aerosol within a comprehensive air quality model system, Journal of
823 Geophysical Research: Atmospheres (1984–2012), 106, 28275-28293, 2001.
824 Skamarock, W. C., Klemp, J. B., Dudhia, J., Gill, D. O., Barker, D. M., Duda, M. G., Huang, X.-Y.,
825 Wang, W., and Powers, J. G.: A Description of the Advanced Research WRF Version 3, NCAR
826 Technical Note, NCAR/TN-475+STR, 2008.
827 Stelson, A. W.: Urban aerosol refractive index prediction by partial molar refraction
828 approach, Environmental Science & Technology, 24, 1676-1679, 10.1021/es00081a008,
829 1990.

Sullivan, R. C., Petters, M. D., DeMott, P. J., Kreidenweis, S. M., Wex, H., Niedermeier, D., Hartmann, S., Clauss, T., Stratmann, F., Reitz, P., Schneider, J., and Sierau, B.: Irreversible loss of ice nucleation active sites in mineral dust particles caused by sulphuric acid condensation, Atmospheric Chemistry and Physics, 10, 11471-11487, 10.5194/acp-10-11471-2010, 2010.

Tegen, I., Lacis, A. A., and Fung, I.: The influence on climate forcing of mineral aerosols from disturbed soils, Nature, 380, 419-422, 10.1038/380419a0, 1996.

Tewari, M., Chen, F., Kusaka, H., and Miao, S.: Coupled WRF/Unified Noah/urban-canopy modeling system, NCAR WRF Documentation, NCAR, Boulder, 1-22, 2007.

Twomey, S.: POLLUTION AND PLANETARY ALBEDO, Atmospheric Environment, 8, 1251-1256, 10.1016/0004-6981(74)90004-3, 1974.

Yang, F.: Radiative forcing and climate impact of the Mount Pinatubo volcanic eruption. , PhD, University of Illinois at Urbana-Champaign., 2000.

Yang, M., Howell, S. G., Zhuang, J., and Huebert, B. J.: Attribution of aerosol light absorption to black carbon, brown carbon, and dust in China – interpretations of atmospheric measurements during EAST-AIRE, Atmos. Chem. Phys., 9, 2035-2050, 10.5194/acp-9-2035-2009, 2009.

Ying, Q., and Kleeman, M. J.: Effects of aerosol UV extinction on the formation of ozone and secondary particulate matter, Atmospheric Environment, 37, 5047-5068, 2003.

Ying, Q., Lu, J., Allen, P., Livingstone, P., Kaduwela, A., and Kleeman, M.: Modeling air quality during the California Regional PM10/PM2.5 Air Quality Study (CRPAQS) using the UCD/CIT source-oriented air quality model - Part I. Base case model results, Atmospheric Environment, 42, 8954-8966, DOI 10.1016/j.atmosenv.2008.05.064, 2008.

Zaveri, R. A., Easter, R. C., Fast, J. D., and Peters, L. K.: Model for Simulating Aerosol Interactions and Chemistry (MOSAIC), Journal of Geophysical Research: Atmospheres, 113, D13204, 10.1029/2007jd008782, 2008.

Zaveri, R. A., Barnard, J. C., Easter, R. C., Riemer, N., and West, M.: Particle-resolved simulation of aerosol size, composition, mixing state, and the associated optical and cloud condensation nuclei activation properties in an evolving urban plume, Journal of Geophysical Research: Atmospheres, 115, D17210, 10.1029/2009jd013616, 2010.

Zhang, H., DeNero, S. P., Joe, D. K., Lee, H. H., Chen, S. H., Michalakes, J., and Kleeman, M. J.: Development of a source oriented version of the WRF/Chem model and its application to the California regional PM10 / PM2.5 air quality study, Atmos. Chem. Phys., 14, 485-503, 10.5194/acp-14-485-2014, 2014.

Captions of Tables

Table 1. Chemical species that are carried in the AQC/CLDAQC "species" dimension. All species are in concentrations (μg m^{-3}) except for the last two elements (i.e., 39 and 40), which carry the number concentration (# m^{-3}) and radius (m).

Table 2. California Ambient Air Quality Data (CAAQD) station information.

Table 3. Numerical experiment designs for this study.

Table 4. Hourly bias mean and standard deviation (std) in day time and night time of 2-m temperature (T2, °C), water vapor mixing ratio (Q2, g kg-air^{-1}), and net downward shortwave radiative flux (NSF, W m^{-2}) between all experiments and observation from 16 to 18 January 2011. T2 and Q2 are calculated using 24 surface stations and NSF is calculated using 42 CIMIS stations shown in Fig. 4.

Table 5. Mean values of cloud liquid water (Q_c), cloud droplet number (Q_n), surface skin temperature (SKT), net shortwave flux (NSF), latent heat flux (LH) and sensible heat flux (SH) for four experiments over the entire Central Valley during 16 to 18 January 2011.

Table 6. The ratio of AQC number concentration for each bin/source to the total number concentration. The numbers are averaged within the first five model layers during 16 to 18 January 2011.

Table 7. Hourly bias mean and root-mean-square-difference of cloud liquid water (Q_c), cloud droplet number (Q_n), surface skin temperature (SKT), net shortwave flux (NSF), latent heat flux (LH) and sensible heat flux (SH) between internally mixed (I_ARon_CRmod) and source-oriented (S_ARon_CRmod) experiments (internally mixed – source-oriented) during 16 to 18 January 2011.

888
889

890 **Captions of Figures**

891 Figure 1. Cloud physics processes that are involved with cloud particles in the SOWC model
892 with a 6D aerosol variable (AQC) and a 6D cloud variable (CLDAQC) included. Black
893 solid arrow and grey dashed arrow indicate the source and the sink processes of cloud
894 water and 6D CLDAQC, as well as 6D AQC, respectively.

895 Figure 2. MODIS true color image at (a) 1930 UTC 16 January 2011 and (b) 1835 UTC 17
896 January 2011 from Satellite Terra, respectively.

897 Figure 3. The column integrated water vapor (shaded; mm), 850-hPa wind vector, and seal level
898 pressure (contours; hPa) from ECMWF Interim reanalysis at (a) 0000 UTC (4 pm local
899 time) 11 January, (b) 0000 UTC 12 January, (c) 0000 UTC 13 January, (d) 0000 UTC 14
900 January, (e) 0000 UTC 15 January, (f) 0000 UTC 16 January, (g) 0000 UTC 17 January,
901 and (h) 0000 UTC 18 January, 2011.

902 Figure 4. NOAA's National Climatic Data Center (NCDC; 24 stations, red dots), California
903 Irrigation Management Information System (CIMIS; 42 stations, black dots) and
904 California Ambient Air Quality Data (6 stations, numbers corresponding to Table 2
905 station ID) measurement locations. Shaded is terrain height in m.

906 Figure 5. The 72-hour averaged (16 to 18 January 2011) AQC number concentration averaged
907 over the first five model layers from the polluted experiment (S_ARon_CRmod) in units
908 of 10^8 # m^{-3}. Contours are terrain heights in m.

909 Figure 6. Comparison of (a) Nitrate (NO_3^-), (b) Sulfate (SO_4^{2-}), (c) Ammonium (NH_4^+), and (d)
910 Soluble Sodium (Na^+) between simulated source-oriented experiment
911 (S_ARon_CRmod), internally mixed experiment (I_ARon_CRmod) and the observed

912 concentrations of airborne particles on 18 January 2011. Units are μg m^{-3}.

913 Figure 7. Liquid water path (LWP) (g m^{-2}) from MODIS Level 2 cloud products ((a), (c) and (e))
914 and from the SOWC model with aerosol feedback on and modified cloud-radiation
915 scheme (S_ARon_CRmod; (b), (d) and (f)). (a) and (b) are at 1900 UTC 16 January
916 2011. (c) and (d) are at 1800 UTC 17 January 2011. (e) and (f) are at 1900 UTC 18
917 January 2011. Contours in (b), (d) and (f) are terrain heights in m.

918 Figure 8. Same as Figure 5 but cloud optical thickness (COT) (dimensionless).

919 Figure 9. Mean bias variation of (a) 2-m temperature (T2), (b) 2-m water vapor mixing ratio
920 (Q2), and (c) surface net downward shortwave radiative flux (NSF) between
921 observations and model simulation from 16 to 18 January 2011 for S_ARon_CRmod
922 (blue lines), S_ARoff_CRmod (purple lines) and I_ARon_CRmod (red lines)
923 experiments.

924 Figure 10. N_{CCN}/N_{CN} ratio for (a) S_ARon_CRmod (source-oriented experiment) and (b)
925 I_ARon_CRmod (internally mixed experiment) averaged within the first five model
926 layers. The ratio is hourly average during 16 to 18 January 2011. Contours are terrain
927 heights in m.

928 Figure 11. (a) 72-hour averaged CCN concentration at supersaturation of 0.02%, 0.05%, 0.1%,
929 0.2%, 0.5% and total AQC concentration with units in # cm^{-3}. (b) N_{CCN}/N_{CN} ratio at 5
930 corresponding supersaturation. Dark gray is source-oriented experiment and light gray
931 represents internally mixed experiment. Results are average values using data within the
932 first five model layers.

933 Figure 12. Relative change ((internally mixed – source-oriented)/source-oriented * 100%) in 72-
934 hour averaged predictions during 16 to 18 January 2011 for (a) the ratio of cloud liquid

935 water, (b) cloud droplet number, (c) surface skin temperature and (d) net shortwave
936 radiation. (a) and (b) are average values using data within the first five model layers.
937 Contours are terrain heights in m.
938 Figure 13. Area average of latent heat flux (LH) and sensible heat flux (SH) over the Central Valley
939 in S_ARon_CRmod and the average difference between I_ARon_CRmod and
940 S_ARon_CRmod from 0800 UTC 17 January (00 Z local time) to 0700 UTC 18 January (23
941 Z local time).
942
943

Table 1. Chemical species that are carried in the AQC/CLDAQC "species" dimension. All species are in concentrations (μg m^{-3}) except for the last two elements (i.e., 39 and 40), which carry the number concentration (# m^{-3}) and radius (m).

	Chemical species		Chemical species
1	EC	21	SOA from lumped Alkane 1
2	OC	22	SOA from lumped Alkane 2
3	NA	23	SOA from lumped Aromatic 1
4	CL	24	SOA from lumped Aromatic 2
5	N3	25	SOA from lumped Aromatic 1
6	S6	26	SOA from lumped Aromatic 2
7	N5	27	SOA from lumped Aromatic 1
8	Other	28	SOA from lumped Aromatic 2
9	Metal	29	SOA from lumped Alkene 1
10	Unknown	30	SOA from lumped Alkene 2
11	CU1	31	SOA from lumped Alpha Pinene 1
12	CU2	32	SOA from lumped Alpha Pinene 2
13	MN2	33	SOA from lumped Beta Pinene 1
14	MN3	34	SOA from lumped Beta Pinene 2
15	FE2	35	SOA from lumped Toluene 1
16	FE3	36	SOA from lumped Toluene 2
17	S4	37	Hydrogen Ion
18	Air (hollow sea salt particles)	38	Water
19	NO3	39	Number Concentration
20	Non-explicit SOA	40	Particle Mean Volume Radius

951

952

953

954

955 Table 2. California Ambient Air Quality Data (CAAQD) station information

Station ID	Station name	Longitude (^{o})	Latitude (^{o})
1	San Jose-Jackson Street	-121.89	37.35
2	Bakersfield-5558 Cal. Avenue	-119.06	35.36
3	Fresno-1st Street	-119.77	36.78
4	Modesto-14th Street	-120.99	37.64
5	Visalia-N Church Street	-119.29	36.33
6	Sacramento-T Street	-121.49	38.57

956

957 Table 3. Numerical experiment designs for this study.

Experiments	Description
S_ARon_CRmod	Source-Oriented aerosols with aerosol direct effect calculation on and modified cloud radiation parameterization
S_ARon_CRorig	Source-Oriented aerosols with aerosol direct effect calculation on and original cloud radiation parameterization
S_ARoff_CRmod	Source-Oriented aerosols with aerosol direct effect calculation off and modified cloud radiation parameterization
I_ARon_CRmod	Internal mixing aerosols with aerosol direct effect calculation on and modified cloud radiation parameterization

958

Table 4. Hourly bias mean and standard deviation (std) in day time and night time of 2-m temperature (T2, °C), water vapor mixing ratio (Q2, g kg-air^{-1}), and net downward shortwave radiative flux (NSF, W m^{-2}) between all experiments and observation from 16 to 18 January 2011. T2 and Q2 are calculated using 24 surface stations and NSF is calculated using 42 CIMIS stations shown in Fig. 4.

	S_ARon_CRmod		S_ARon_CRorig		S_ARoff_CRmod		I_ARon_CRmod	
Daytime	Bias mean	std	Bias mean	std	Bias mean	std	Bias mean	std
T2	-1.76	1.27	-1.72	1.32	-1.63	1.33	-2.01	1.09
Q2	-0.56	0.34	-0.56	0.36	-0.54	0.35	-0.57	0.32
NSF	13.91	53.18	14.40	58.00	18.81	58.78	8.68	50.03
Nighttime	Bias mean	std	Bias mean	std	Bias mean	std	Bias mean	std
T2	-2.22	0.92	-2.21	0.95	-2.19	0.93	-2.30	0.87
Q2	-0.88	0.41	-0.87	0.42	-0.88	0.42	-0.89	0.41
NSF	/	/	/	/	/	/	/	/

966
967 Table 5. Mean values of cloud liquid water (Q_c), cloud droplet number (Q_n), surface skin
968 temperature (SKT), net shortwave flux (NSF), latent heat flux (LH) and sensible heat flux (SH)
969 for four experiments over the entire Central Valley during 16 to 18 January 2011.
970

	S_ARon_CRmod	**S_ARon_CRorig**	**S_AROff_CRmod**	**I_ARon_CRmod**
Q_c^* (g m^{-3})	0.220	0.221	0.213	0.231
Q_n^* (# m^{-3})	3.94×10^8	4.18×10^8	3.77×10^8	4.57×10^8
SKT (K)	281.305	281.30	281.404	281.151
NSF** (W m^{-2})	130.56	131.02	134.24	124.54
LH (W m^{-2})	9.01	9.02	9.36	8.40
SH (W m^{-2})	4.91	4.55	5.27	4.54
COT (unitless)	25.56	25.15	24.49	28.62

971 * Averaged within the first five model layers
972 ** Averaged only in the daytime

973

974 Table 6. Ratio of AQC number concentration for each bin/source to the total number
975 concentration. The numbers are averaged within the first five model layers during 16 to 18
976 January 2011.

	Wood smoke	Gasoline	Diesel	Meat cooking	Others	Source-oriented	Internal
Bin1	28.92%	1.00%	4.25%	0.84%	10.39%	45.40%	48.89%
Bin2	9.12%	0.38%	1.48%	0.60%	38.64%	50.22%	46.74%
Bin3	0.19%	0.01%	0.03%	0.02%	3.03%	3.28%	3.26%
Bin4	0.00%	0.00%	0.00%	0.00%	0.17%	0.18%	0.21%
Bin5	0.00%	0.00%	0.00%	0.00%	0.02%	0.02%	0.02%
Bin6	0.00%	0.00%	0.00%	0.00%	0.00%	0.00%	0.00%
Bin7	0.00%	0.00%	0.00%	0.00%	0.00%	0.00%	0.00%
Bin8	0.00%	0.00%	0.00%	0.00%	0.91%	0.91%	0.88%

977

978 Table 7. Hourly bias mean and root-mean-square-difference of cloud liquid water (Q_c), cloud
979 droplet number (Q_n), surface skin temperature (SKT), net shortwave flux (NSF), latent heat flux
980 (LH) and sensible heat flux (SH) between internally mixed (I_ARon_CRmod) and source-
981 oriented (S_ARon_CRmod) experiments (internally mixed – source-oriented) during 16 to 18
982 January 2011.

	Bias mean	**Root-mean-square-difference**
Q_c^* (g m^{-3})	1.19×10^{-2}	4.16×10^{-2}
Q_n^* (# m^{-3})	6.24×10^{7}	2.64×10^{8}
SKT (K)	-0.15	0.57
NSF (W m^{-2})	-6.02	13.30
LH (W m^{-2})	-0.61	2.75
SH (W m^{-2})	-0.36	5.24

983 * Averaged within the first five model layers

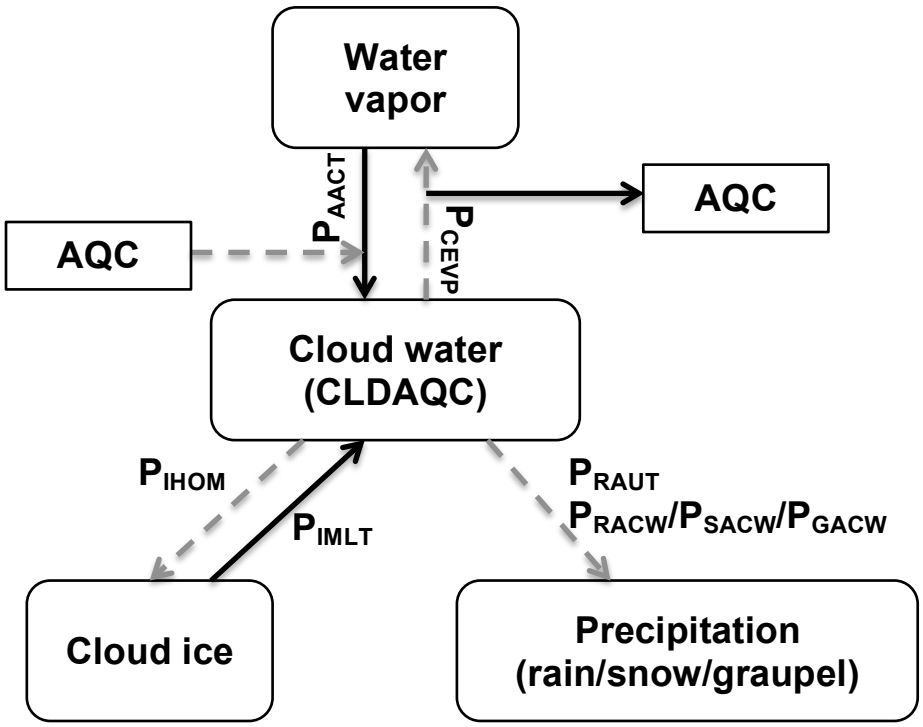

Figure 1. Cloud physics processes that are involved with cloud particles in the SOWC model with a 6D aerosol variable (AQC) and a 6D cloud variable (CLDAQC) included. Black solid arrow and grey dashed arrow indicate the source and the sink processes of cloud water and 6D CLDAQC, as well as 6D AQC, respectively.

(a)

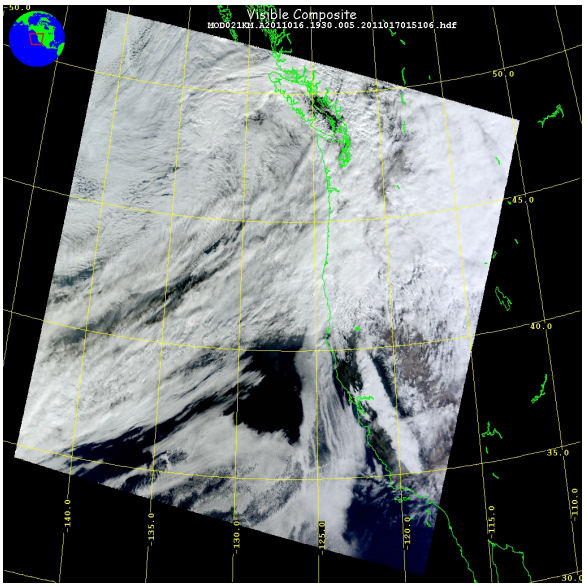

(b)

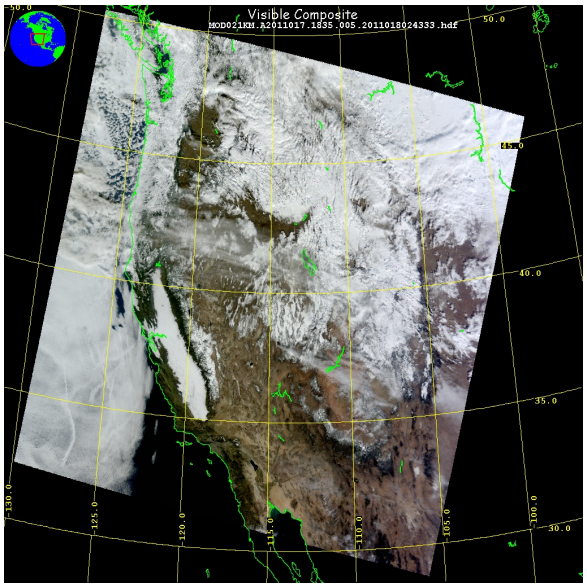

(c)

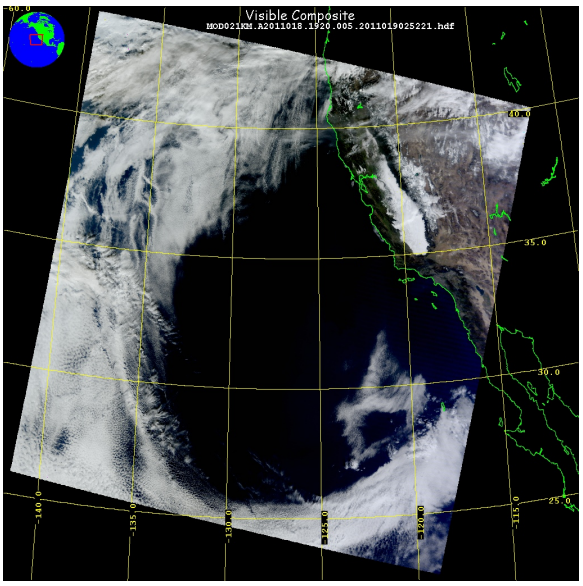

Figure 2. MODIS true color images at (a) 1930 UTC 16 January, (b) 1835 UTC 17 January, and (c) 1920 UTC 18 January, 2011 from Satellite Terra.

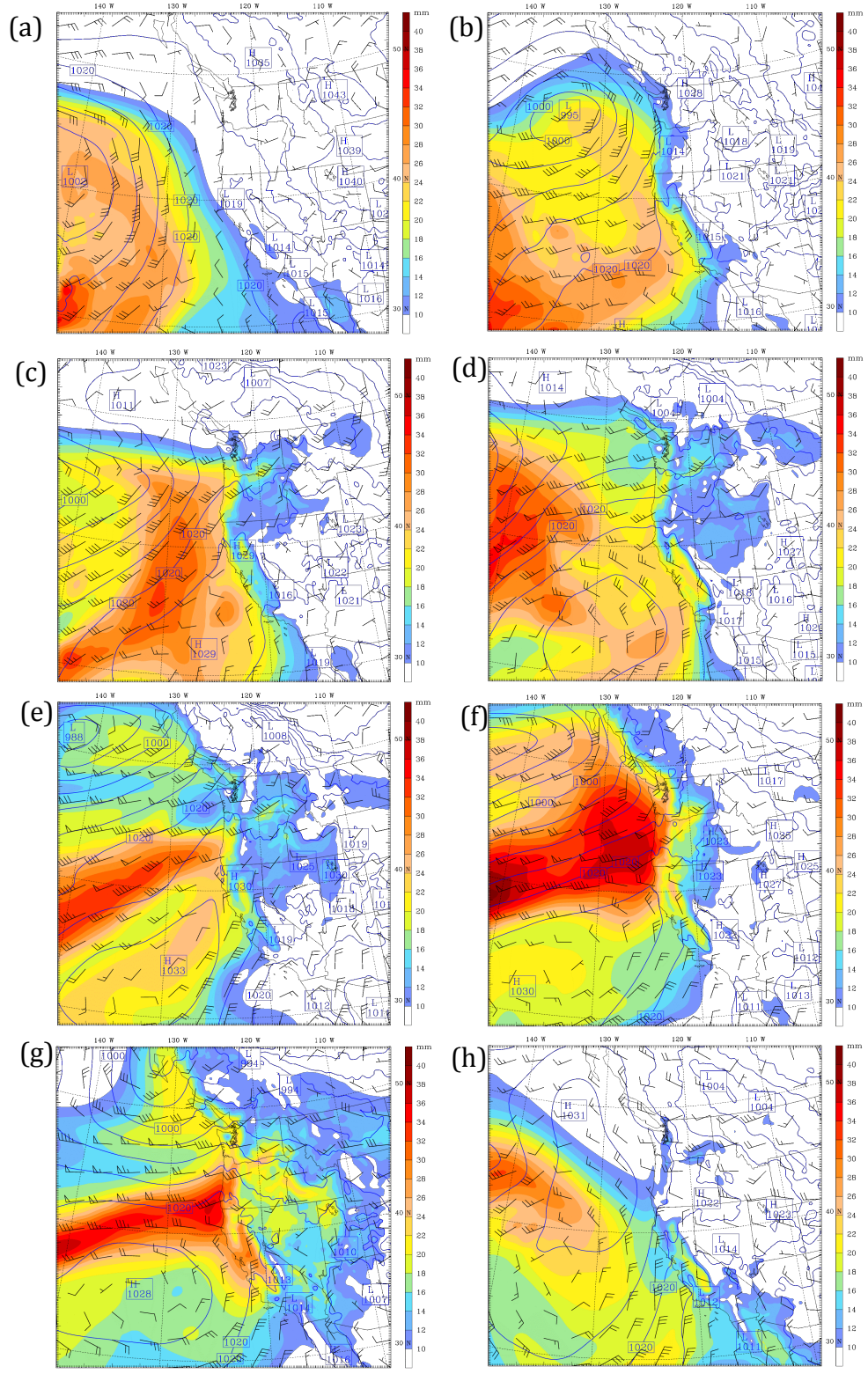

Figure 3. The column integrated water vapor (shaded; mm), 850-hPa wind vector, and sea level pressure (contours; hPa) from ECMWF Interim reanalysis at (a) 0000 UTC (4 pm local time) 11

January, (b) 0000 UTC 12 January, (c) 0000 UTC 13 January, (d) 0000 UTC 14 January, (e) 0000 UTC 15 January, (f) 0000 UTC 16 January, (g) 0000 UTC 17 January, and (h) 0000 UTC 18 January, 2011.

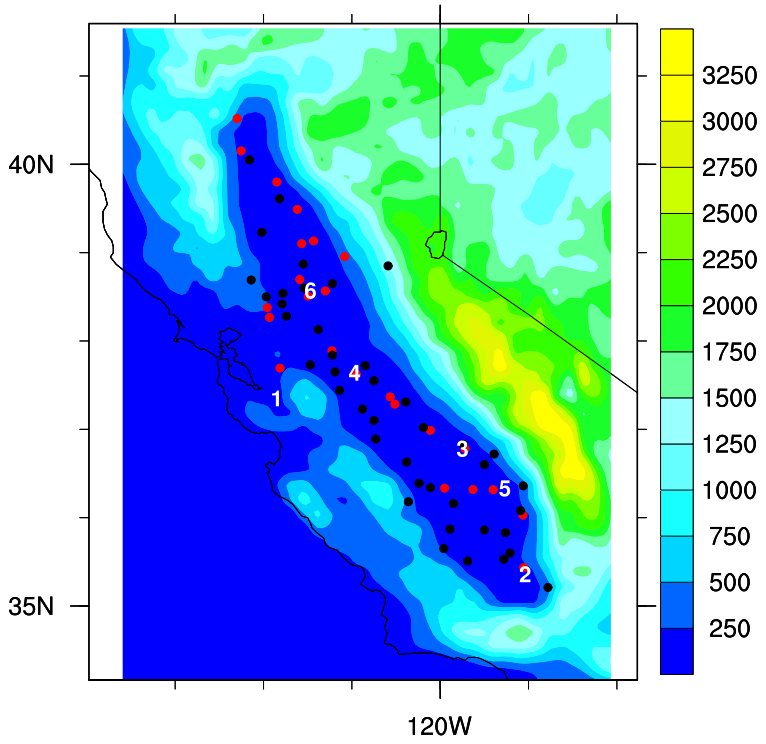

Figure 4. NOAA's National Climatic Data Center (NCDC; 24 stations, red dots), California Irrigation Management Information System (CIMIS; 42 stations, black dots) and California Ambient Air Quality Data (6 stations, numbers corresponding to Table 2 station ID) measurement locations. Shaded is terrain height in m.

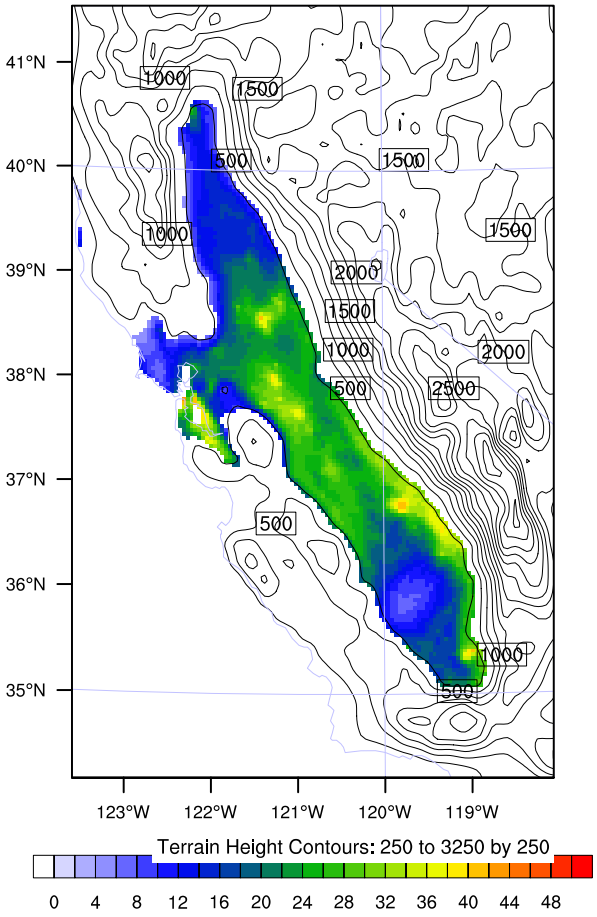

Figure 5. The 72-hour averaged (16 to 18 January 2011) AQC number concentration averaged over the first five model layers from the experiment S_ARon_CRmod in units of 10^8 # m^{-3}. Contours are terrain heights in m.

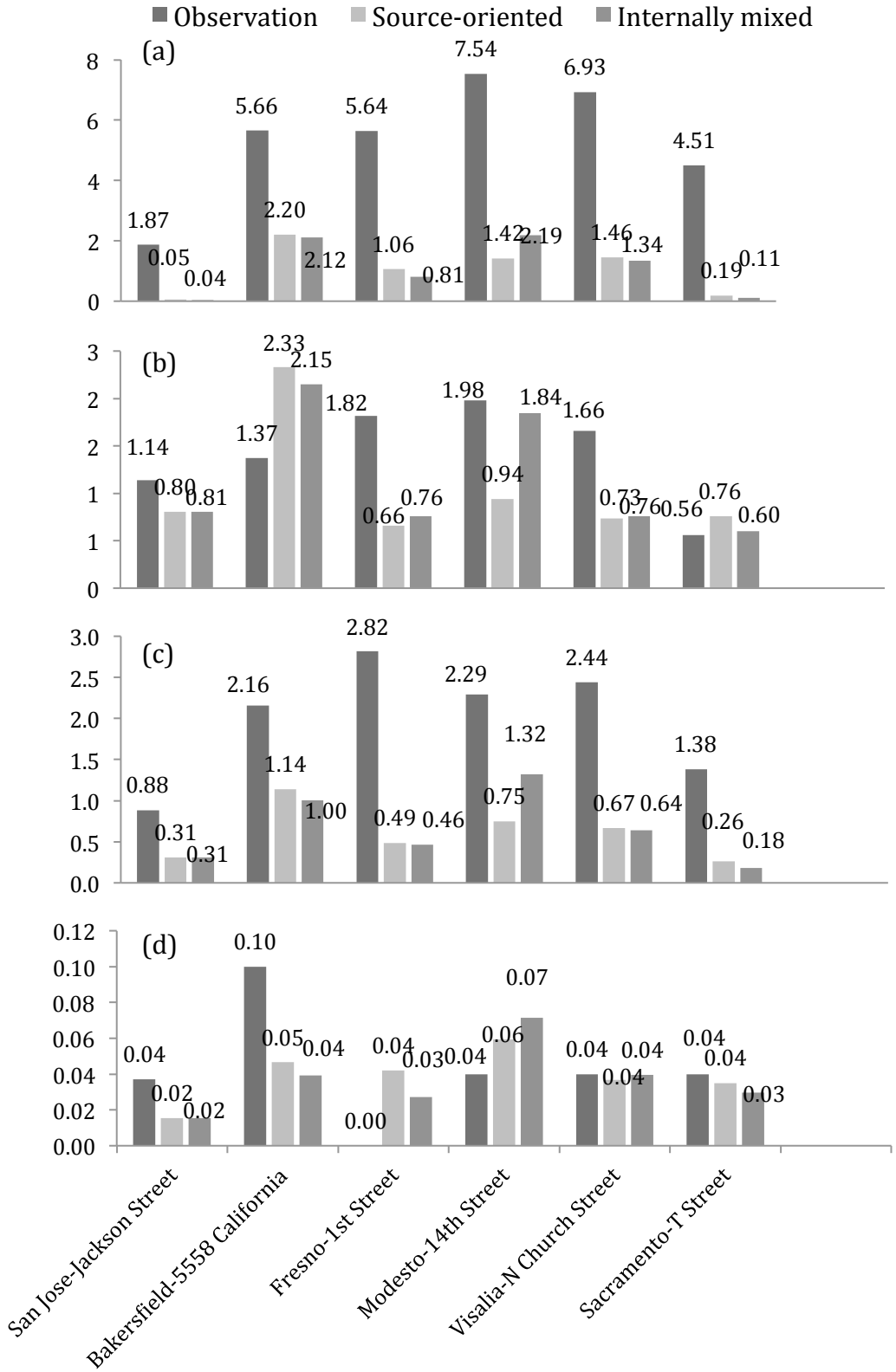
Observation
Source-oriented
Internally mixed
(a)
1.87
0.05
0.04
5.66
2.20
2.12
5.64
1.06
0.81
7.54
1.42
2.19
6.93
1.46
1.34
4.51
0.19
0.11
(b)
1.14
0.80
0.81
1.37
2.33
2.15
1.82
0.66
0.76
1.98
0.94
1.84
1.66
0.73
0.76
0.56
0.76
0.60
(c)
0.88
0.31
0.31
2.16
1.14
1.00
2.82
0.49
0.46
2.29
0.75
1.32
2.44
0.67
0.64
1.38
0.26
0.18
(d)
0.04
0.02
0.02
0.10
0.05
0.04
0.00
0.04
0.03
0.04
0.06
0.07
0.04
0.04
0.04
0.04
0.04
0.03
San Jose-Jackson Street
Bakersfield-5558 California
Fresno-1st Street
Modesto-14th Street
Visalia-N Church Street
Sacramento-T Street

Figure 6. Comparison of (a) Nitrate (NO_3^-), (b) Sulfate (SO_4^{2-}), (c) Ammonium (NH_4^+), and (d) Soluble Sodium (Na^+) between simulated source-oriented experiment (S_ARon_CRmod), internally mixed experiment (I_ARon_CRmod) and the observed concentrations of airborne particles on 18 January 2011. Units are μg m^{-3}.

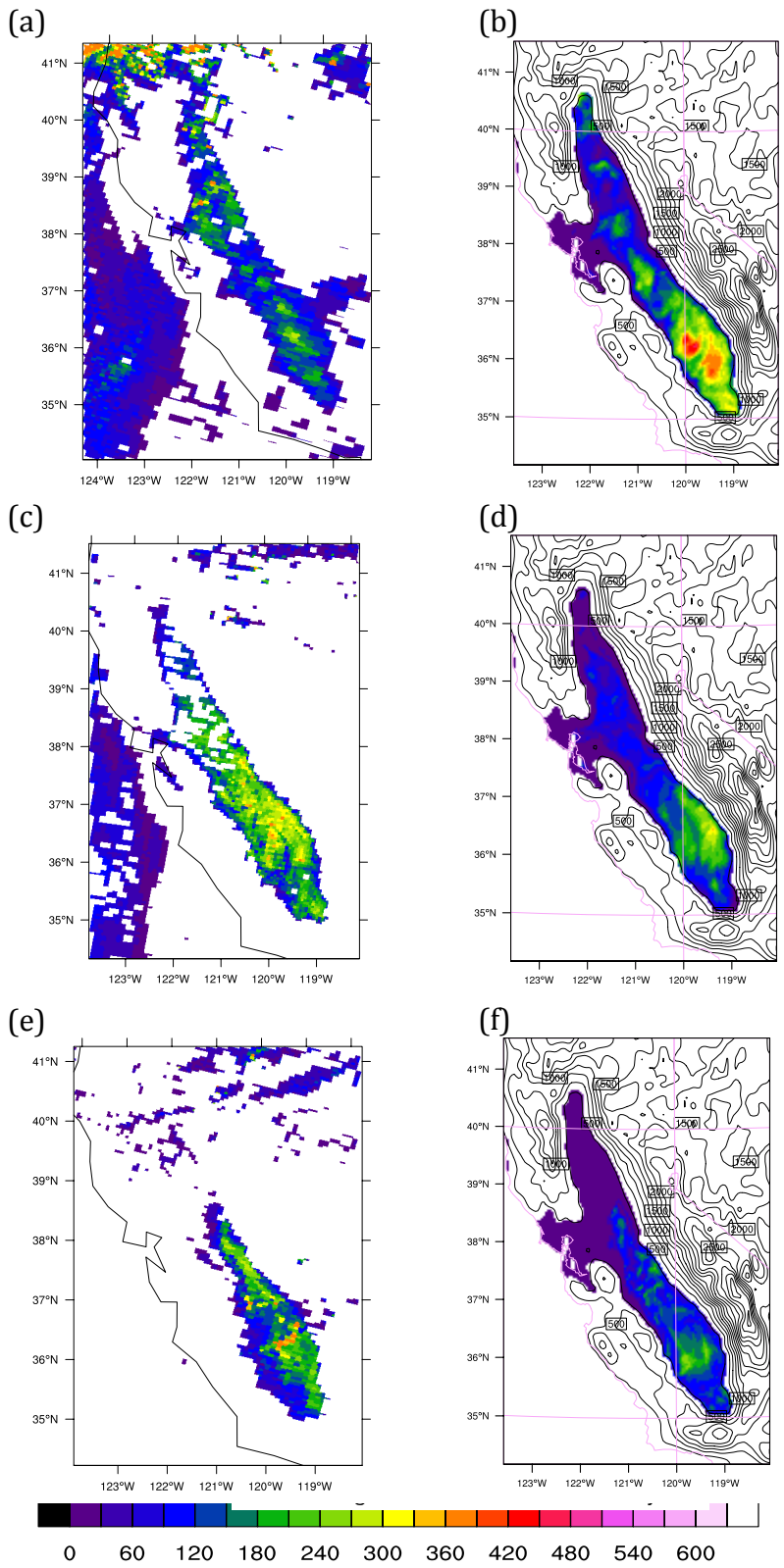

Figure 7. Liquid water path (LWP) (g m^{-2}) from MODIS Level 2 cloud products ((a), (c) and (e)) and from the SOWC model with aerosol feedback on and modified cloud-radiation scheme (S_ARon_CRmod; (b), (d) and (f)). (a) and (b) are at 1900 UTC 16 January 2011. (c) and (d) are

1122 at 1800 UTC 17 January 2011. (e) and (f) are at 1900 UTC 18 January 2011. Contours in (b), (d)
1123 and (f) are terrain heights in m.
1124

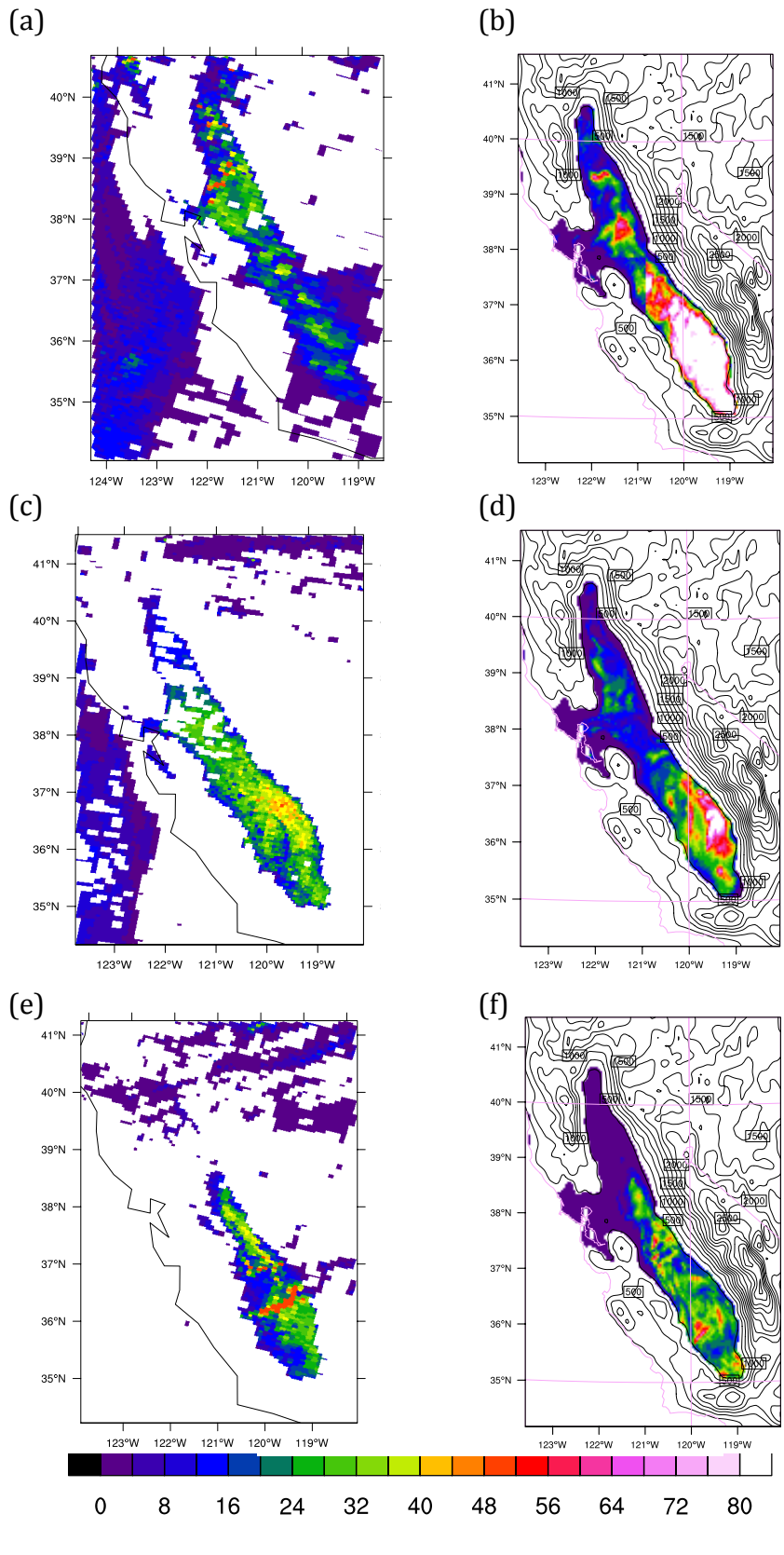
(a)
(b)
(c)
(d)
(e)
(f)
0
8
16
24
32
40
48
56
64
72
80

1134 Figure 8. Same as Figure 5 but cloud optical thickness (COT) (dimensionless).
1135
1136
1137

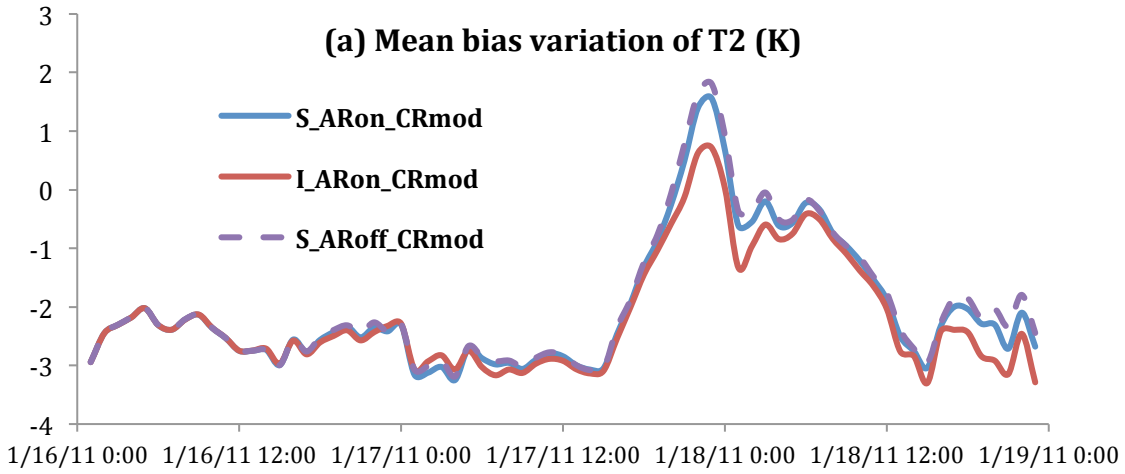

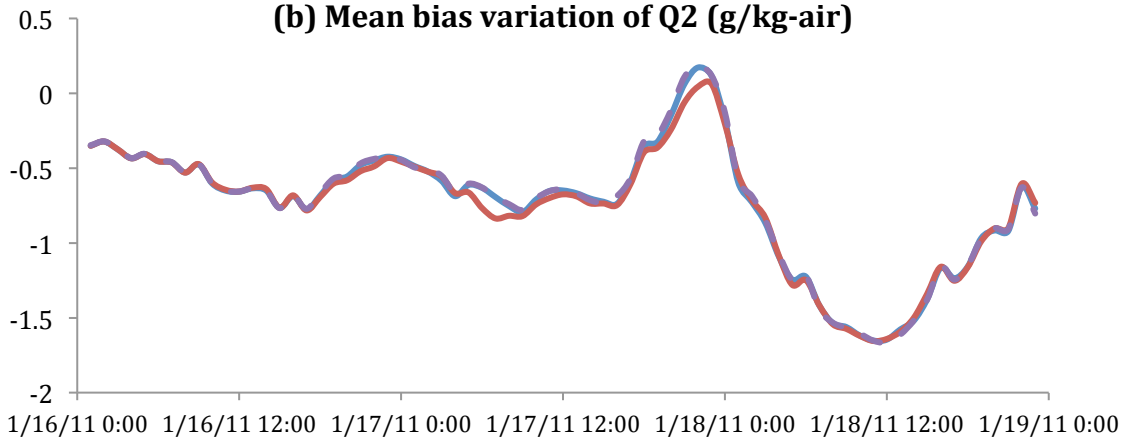

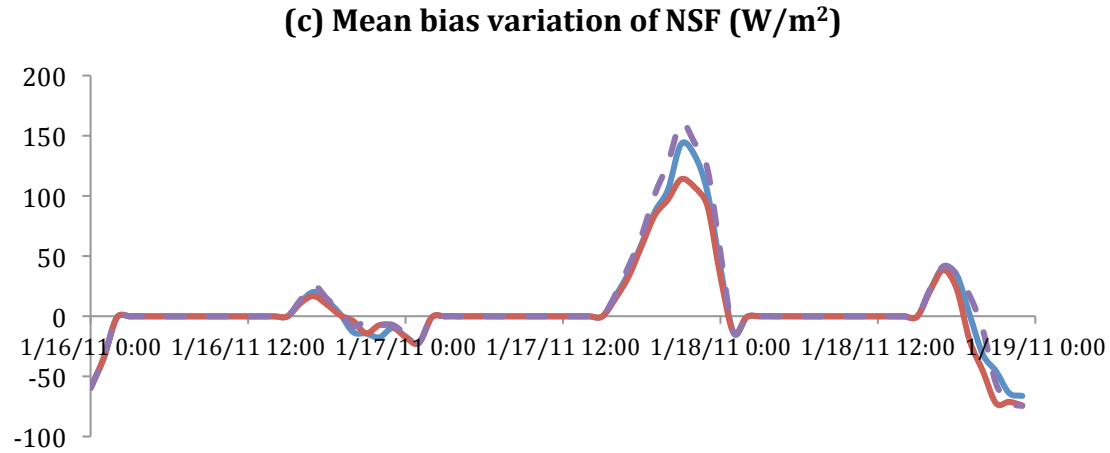

Figure 9. Mean bias variation of (a) 2-m temperature (T2), (b) 2-m water vapor mixing ratio (Q2), and (c) surface net downward shortwave radiative flux (NSF) between observations and model simulation from 16 to 18 January 2011 for S_ARon_CRmod (blue lines), S_ARoff_CRmod (purple lines) and I_ARon_CRmod (red lines) experiments.

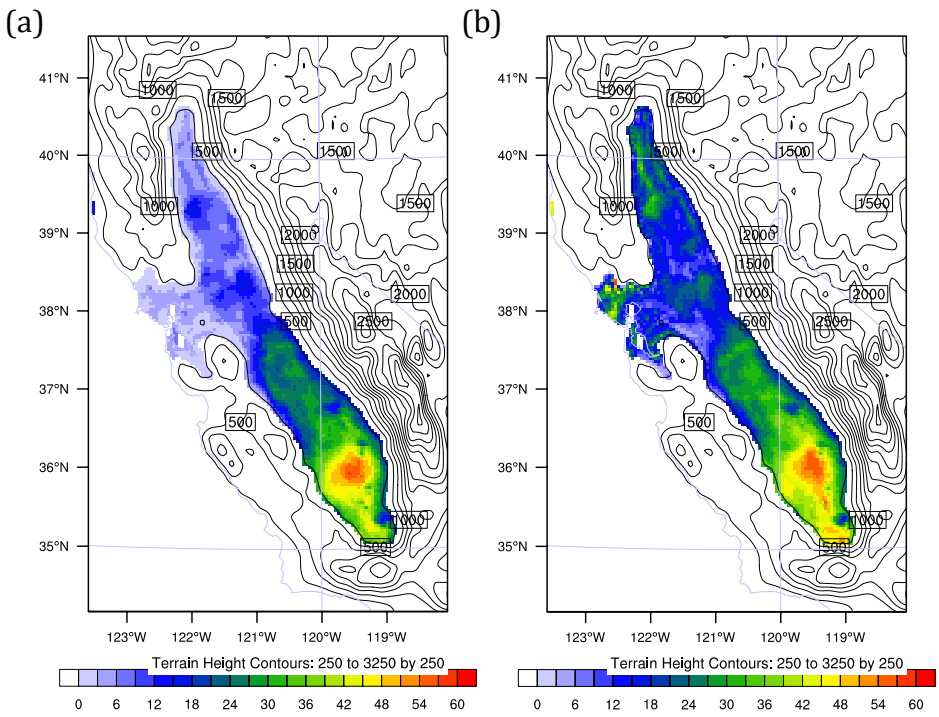

Figure 10. N_{CCN}/N_{CN} ratio for (a) S_ARon_CRmod (source-oriented experiment) and (b) I_ARon_CRmod (internally mixed experiment) averaged within the first five model layers. The ratio is hourly average during 16 to 18 January 2011. Contours are terrain heights in m.

1157

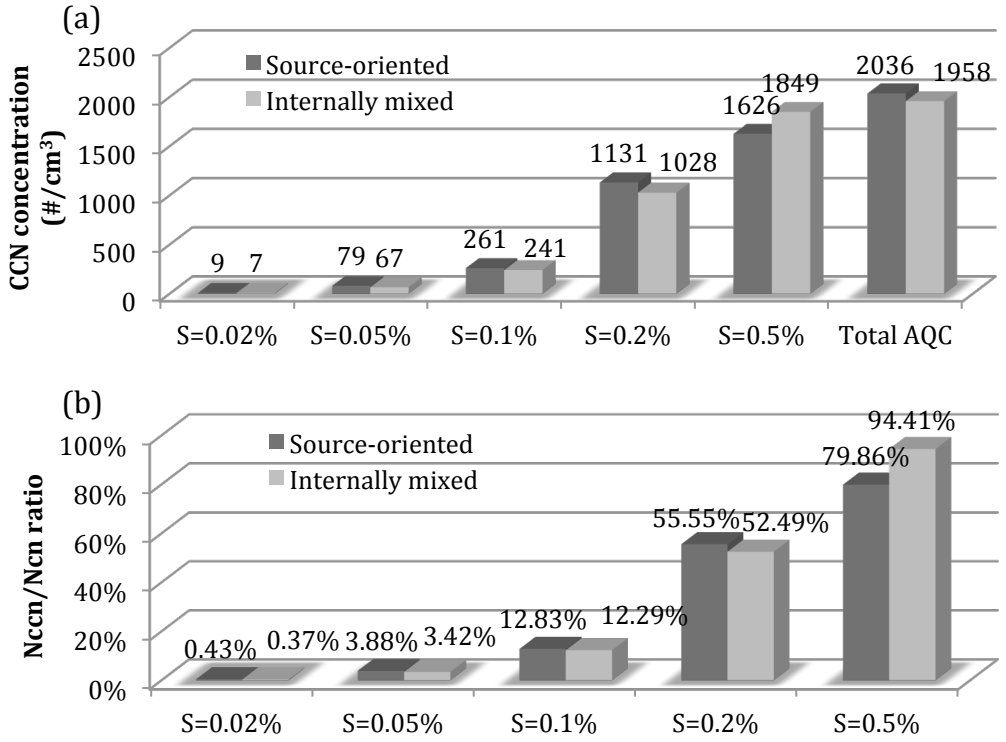

1158

1159

1160

1161 Figure 11. (a) 72-hour averaged CCN concentration at supersaturation of 0.02%, 0.05%, 0.1%,
1162 0.2%, 0.5% and total AQC concentration with units in # cm^{-3}. (b) N_{CCN}/N_{CN} ratio at 5
1163 corresponding supersaturation. Dark gray is source-oriented experiment and light gray represents
1164 internally mixed experiment. Results are average values using data within the first five model
1165 layers.

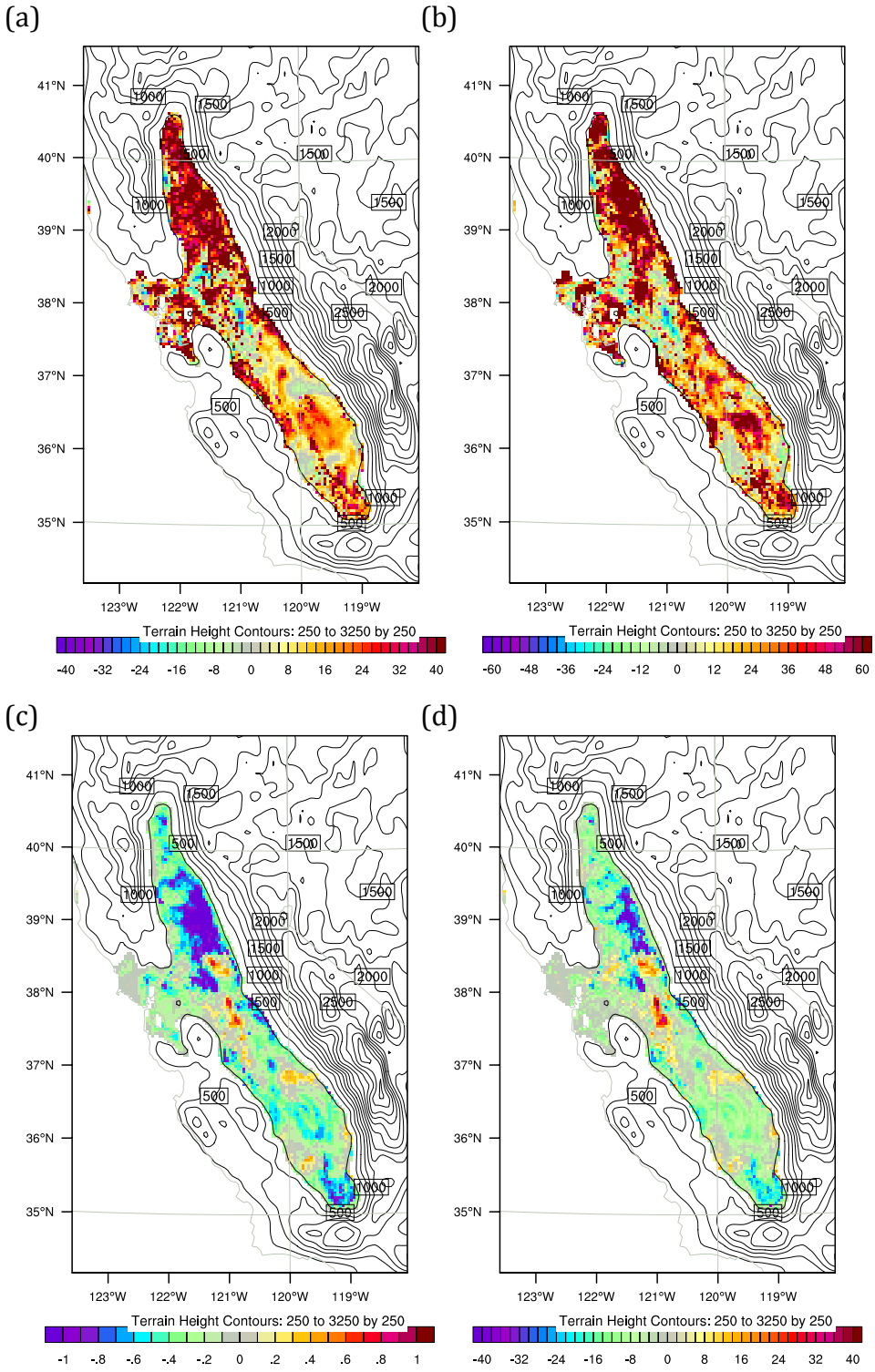

Figure 12. Relative change ((internally mixed – source-oriented)/source-oriented * 100%) in the daytime averaged predictions during 16 to 18 January 2011 for (a) the ratio of cloud liquid water,

(b) cloud droplet number and absolute difference (internally mixed – source-oriented) in (c) surface skin temperature (K) and (d) net shortwave radiation (W m^{-2}). (a) and (b) are average values using data within the first five model layers. Contours are terrain heights in m.

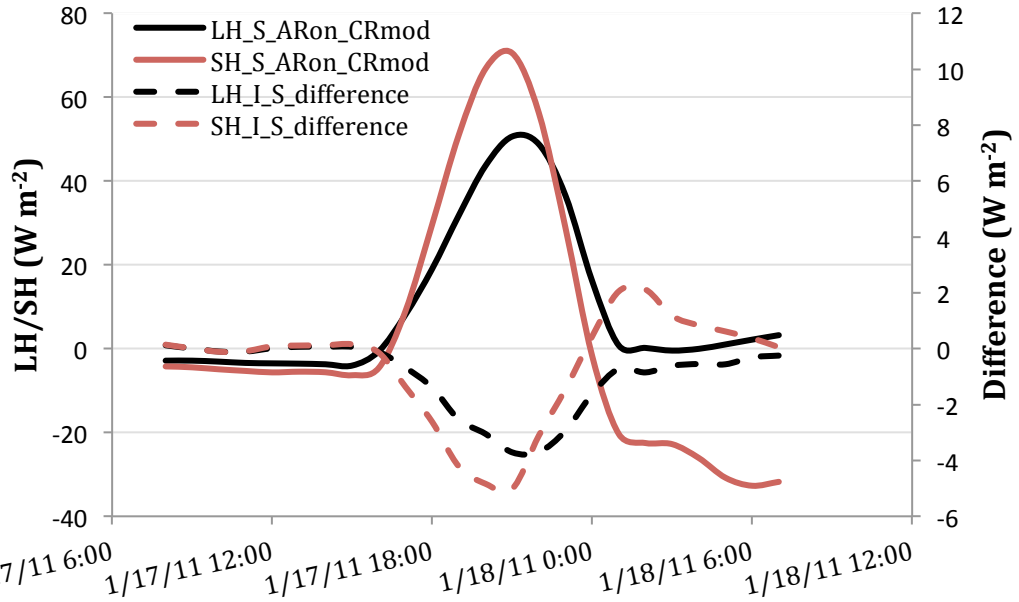

Figure 13. Area average of latent heat flux (LH) and sensible heat flux (SH) over the Central Valley in S_ARon_CRmod and the average difference between I_ARon_CRmod and S_ARon_CRmod from 0800 UTC 17 January (00 Z local time) to 0700 UTC 18 January (23 Z local time).